School of Industrial and Information Engineering
Master of Science in Engineering Physics

POLITECNICO
MILANO 1863

Synthesis and characterization of 2D h-BN/graphene heterostructures grown by Chemical Vapor Deposition

Supervisor: Prof. Roman Sordan
Co-Supervisors: Dr. Amaia Zurutuza and Alba Centeno

Author:
Stefano Atella Matr. 837223

Accademic Year 2016-2017

Summary

This thesis work has been entirely done at GRAPHENEA, a worldwide company in the production of graphene and in the development of related research. The main objective is the growth, manufacture and characterization of hexagonal boron nitride (h-BN) and graphene. In particular, the construction of this structures will occur with an alternative method which involves a significant reduction of dopant impurities due to the use of polymers (specifically PMMA) necessary for the transfer process: this transfer process takes the name of *PMMA free interface transfer process*. Such heterostructures can then be subjected to optical lithography for the fabrication of electrical devices for the measurement of the most important graphene electronic parameters as e.g. electronic mobility. The first part of the thesis (Chapters 1, 2) consists of a theoretical introduction to graphene and h-BN, with its bandstructure, a Graphene Field Effect Transistor (GFET) theoretical model and state-of-the art of the research and possible applications. Subsequently, Chapters 3 and 4 describe the Chemical Vapor Deposition (CVD) process for the production of graphene together with the characterization with several laboratory techniques (optical characterization, AFM, Raman, IR, TEM). In addition, characterization will also be performed on commercial CVD h-BN samples. In Chapter 5, however, h-BN production is discussed in detail through CVD: in particular, a possible instrument setup will be illustrated as well as growth conditions and the analysis of the material obtained. Finally, in the last part, the standard multitransfer process used in order to build such heterostructures is compared with the suggested transfer process: the results obtained using the optical microscope will highlight a significant reduction in PMMA contamination in the h-BN/graphene interface.

Il presente lavoro di tesi stato interamente svolto presso l'azienda GRAPHENEA, azienda a livello mondiale nella produzione di grafene e nello sviluppo della ricerca ad esso connessa. Il lavoro si pone come obiettivo primario, la crescita, la fabbricazione e la caratterizzazione di eterostrutture composte da nitruro di boro esagonale (h-BN) e grafene. In particolare, la realizzazione di tale strutture avverrá con un metodo alternativo che prevede una riduzione significativa di impurezze droganti dovute all'utilizzo di polimeri (nello specifico, PMMA) necessari al processo di transfer: tale processo di transfer prende il nome di *PMMA free interface transfer process*. Tali eterostrutture, potranno poi essere sottoposte a litografia ottica per la realizzazione di *devices* per la misurazione dei pi importanti parametri elettronici del grafene, primo fra tutti, la mobilitá elettronica. La prima parte della tesi, (Capitoli 1, 2) consiste in un'introduzione teorica al grafene e all'h-BN, con la struttura a bande, un modello teorico di Graphene Field effect Transistor (GFET) e lo stato dell'arte della ricerca e delle possibili applicazioni. Successivamente, nei Capitoli 3 e 4, viene descritto il processo di Chemical Vapor Deposition (CVD) per la produzione di grafene insieme alla caratterizzazione con numerose tecniche di laboratorio (caratterizzazione ottica, AFM, Raman, IR, TEM) dello stesso. Inoltre, la caratterizzazione verrá effettuata anche su dei campioni di CVD h-BN commerciali. Nel Capitolo 5 invece, viene affrontata in dettaglio la produzione di h-BN tramite CVD: in particolare, verr illustrato il *setup* della strumentazione, le condizioni di crescita e l'analisi del materiale ottenuto. Infine, nell'ultima parte, viene comparato il normale processo standard di *multitransfer* per la realizzazione di eterostrutture, con il nuovo processo di transfer: i risultati al microscopio ottico, evidenzieranno una significativa riduzione della contaminazione da PMMA all'interfaccia h-BN/grafene.

Acknowledgements

First of all I would like to thank Prof. Roman Sordan for giving me the opportunity to discover the magic world of graphene and sharing with me, and all the other students of the "Semiconductor Nanotechnologies" class, part of his knowledge.

A huge and indispensable thanks goes to the Graphenea's team (*el mejor equipo del mundo...*) to have welcomed me as if I have always been one of you and for believing in me right away. You have given me the opportunity to live 6 months intense during which I grew up not only from the point of view of knowledge but also as a man. At the end of this experience, I realized that I did not have work colleagues but real friends. So thank you, thank you and thank you again. However, I think that a little bigger thanks (just a bit, in order to not appear as a real *pelota*...) goes to Alba who had too much patience with me but who always helped me and spurred me with the smile and who strongly believed in the good outcome of this thesis.

A heartfelt thanks to Karin for having given me this year and a half the urge, but above all, the tranquility to face the examinations and the difficulties that only a degree in engineering can encounter. You made me feel important to someone and this is the thing I needed the most.

Thanks to all my friends, the historical ones and those I've known in recent years. You have been and you will be the most fun side of what it was and what it will be.

My experience at Politecnico came to the end. During these six years (almost seven) I have had both exciting moments and really difficult moments. Here, in this regard, I believe that an infinite thank you goes to my family who never failed to support me and always motivated me to push me beyond my limits. If it had not been for them this path would never end. And maybe it would never have begun.

I love you.

Figure 1: Graphenea Team, *el mejor equipo del mundo...*

List of Figures

List of Tables

Contents

Chapter 1

Introduction

1.1 A brief history of Graphene

Graphene was the first 2D material being isolated and characterized. In 2004, Andre Geim and Konstantin Novoselov, with the process of mechanical exfoliation (or called "scotch tape" method) of a small quantity of highly oriented pyrolitic graphite, were the first scientists to isolate a single layer of carbon atoms. Their article "*Electric Field Effect in Atomically Thin Carbon Films*" [1], in which they report the effective proof of graphene, was awarded with the Nobel Prize for Physics in 2010 and gave rise to an intense research work, which led the EU to establish the Graphene Flagship project and to finance graphene research with one billion of euros over ten years.

The discovery of graphene aroused special heed in science since it was in contrast with the previous Landau and Peierls' theory stating that 2D materials are thermodynamically unstable below a certain thickness and they are impossible to obtain. For this reason, for many years graphene has been classified as an academic material, in contrast with all the other carbon allotropes such as fullerenes and nanotubes (Figure 1.1).

For 2D crystals, the thermal fluctuations become so relevant that the displacements of the atoms of the crystal from their equilibrium position becomes comparable to the interatomic distance leading to the disintegration of the material. In addition, the melting temperature of thin films rapidly decreases when decreasing the thickness and this make the films become unstable around ten layer of thickness [2]. However, the possibility to isolate a flake of graphene is not in contrast with the Landau and Peierls theory thanks to the presence of corrugations in the third

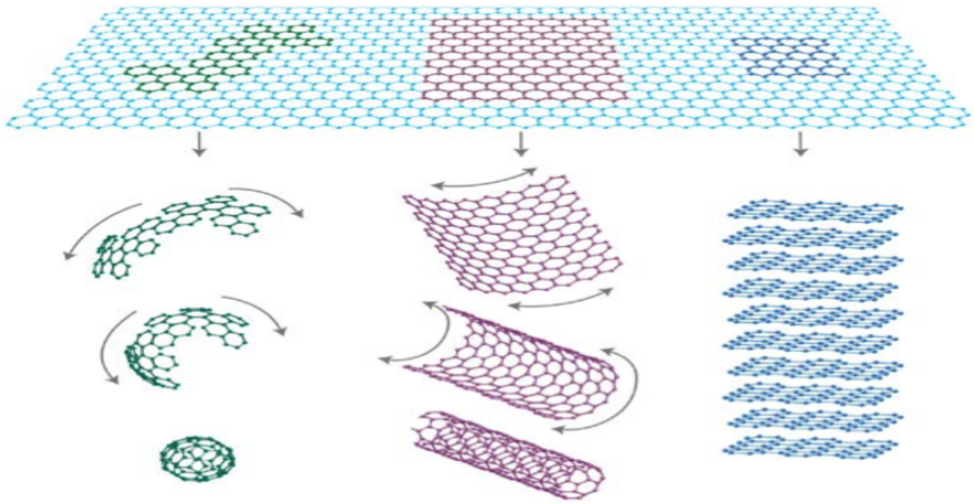

Figure 1.1: Comparison between different carbon structures. On the left fullerens with 12 adjacent pentagons; in the center 1D nanotubes; on the right 2D graphene.

dimension which make the graphene lose the status of perfect bi-dimensional material: interaction between bending and stretching long-wavelength phonons stabilizes a 2D crystal through its deformation in the third dimension.

Since its discovery graphene has been found to be an extraordinary material due to its features: it has exceptional mechanical properties with an intrinsic tensile strength of 130 GPa and a Young modulus of 1 TPa, which make graphene the strongest material ever tested (about 200 times stronger than the strongest steel), and exceptional thermal properties with a thermal conductivity up to $5300 W m^{-1} K^{-1}$; it efficiently conducts electricity with a theoretical mobility at room temperature of $200.000 cm^{-2} V^{-1} s^{-1}$ at a carrier density of $10^{12} cm^{-2}$ and an electrical conductivity of $7200 S m^{-1}$. Graphene is also nearly transparent and shows a large and nonlinear diamagnetism, greater than graphite. These properties make graphene a suitable material for many potential applications: from photonics (photodetectors, optical modulators, mode-locked lasers, THz frequency generators) to electronics (flexible electronics, OLEDs, high-frequency transistors, logic transistors), from metrology up to biomedical applications [3].

1.2 Graphene structure

Graphene is a single atomic sheet of carbon atoms that are arranged in a honeycomb lattice. It can be wrapped up into fullerenes, rolled into 1D nanotubes or stacked into 3D graphite by means of Van der Waals forces (Figure 1.1).

In order to better explain the peculiar structure of graphene, we should take into account the presence of the 4 valence electrons in the $n = 2$ shell of carbon, with an electron configuration of $1s^2 2s^2 2p^2$. Bond formation with closer atom or closer structures depends on the hybridization of valence orbitals, which can assume sp, sp^2 or sp^3 configurations depending on the number of p orbitals involved in the bonding.

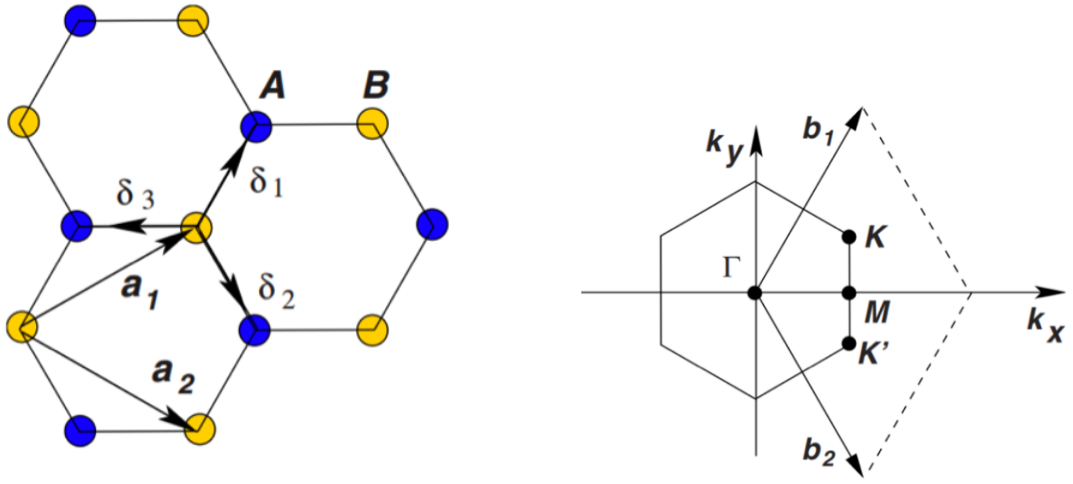

Figure 1.2: Lattice structure of graphene with two interpenetrating triangular lattice and the two lattices vectors **a** and **b** (left); corresponding first Brillouin zone with two equivalent points **K** and **K'** (right) [6].

If the hybridization sp and sp^3 give rise to linear and tetrahedral structures respectively, the hexagonal planar pattern of graphene, or honeycomb, suggests a hybridization of sp^2. s and p orbitals link to form 3σ bonds: since the less energetic configuration is the one with orbitals as far as possible, for such 3 orbitals we will have a planar distribution on a xy plane with angles of 120° such that each carbon atom is around $1.42\mathring{A}$ from its three neighbours. The result is two inequivalent interpenetrated triangular Bravais sublattices A and B (Figure 1.2). The forth electron belongs to the $2p_z$ orbital and is the one forming π bond or π^* antibond which are responsible for many of the most important electronic properties

of graphene.

To explain some of the most fundamental properties of graphene, we will use a tight binding approach. The lattice vectors can be written as [5]:

$$\mathbf{a}_1 = \frac{a}{2}(3, \sqrt{3}) \qquad \mathbf{a}_2 = \frac{a}{2}(3, -\sqrt{3}) \tag{1.1}$$

while the reciprocal-lattice vectors are given by:

$$\mathbf{b}_1 = \frac{2\pi}{3a}(1, \sqrt{3}) \qquad \mathbf{b}_1 = \frac{2\pi}{3a}(1, -\sqrt{3}) \tag{1.2}$$

Each atom of $A(B)$ type (Figure 1.2) is connected to its three nearest neighbors of $B(A)$ type via the displacement vectors:

$$\delta_1 = \frac{a}{2}(1, \sqrt{3}) \qquad \delta_2 = \frac{a}{2}(1, -\sqrt{3}) \qquad \delta_3 = -a(1,0) \tag{1.3}$$

The two equivalent points **K** and **K'**, named Dirac points, are of particular importance for the physics of graphene. Their positions in momentum space are given by:

$$\mathbf{K} = (\frac{2\pi}{3a}, \frac{2\pi}{3\sqrt{3a}}) \qquad \mathbf{K}' = (\frac{2\pi}{3a}, -\frac{2\pi}{3\sqrt{3a}}) \tag{1.4}$$

Calling $|\phi_A(\mathbf{r})\rangle$ and $|\phi_B(\mathbf{r})\rangle$ the atomic wave functions of an atom of the sublattice A and sublattice B respectively, the electron wave function is given by the following linear combination [6]:

$$\begin{aligned} |\Psi(\mathbf{k}, \mathbf{r})\rangle &= \sum_i \psi_A(\mathbf{k}) e^{j\mathbf{k}\mathbf{r}_{Ai}} |\phi_A(\mathbf{r} - \mathbf{r_{ai}})\rangle + \sum_i \psi_B(\mathbf{k}) e^{j\mathbf{k}\mathbf{r}_{Bi}} |\phi_B(\mathbf{r} - \mathbf{r_{Bi}})\rangle \\ &= \psi_A(\mathbf{k}) \sum_i e^{j\mathbf{k}\mathbf{r}_{Ai}} |\phi_A(\mathbf{r} - \mathbf{r_{ai}})\rangle + \psi_B(\mathbf{k}) \sum_i e^{j\mathbf{k}\mathbf{r}_{Bi}} |\phi_B(\mathbf{r} - \mathbf{r_{Bi}})\rangle \end{aligned}$$

which we introduce in the time-independent Schrödinger equation:

$$H|(\mathbf{k}, \mathbf{r})\rangle = E(\mathbf{k})|(\mathbf{k}, \mathbf{r})\rangle \tag{1.5}$$

Multiplying both terms of the equation by $\langle\phi_A(\mathbf{r})|$ first and by $\langle\phi_B(\mathbf{r})|$ then, we arrive at two eigen-equations:

$$-\gamma f(\mathbf{k})\psi_B(\mathbf{k}) = E(\mathbf{k})\psi_A(\mathbf{k})$$
$$-\gamma f^*(\mathbf{k})\psi_A(\mathbf{k}) = E(\mathbf{k})\psi_B(\mathbf{k})$$

In matrix form the previous equation can be rewritten as:

$$\begin{bmatrix} 0 & -\gamma f(\mathbf{k}) \\ -\gamma f^*(\mathbf{k}) & 0 \end{bmatrix} \begin{bmatrix} \psi_A(\mathbf{k}) \\ \psi_B(\mathbf{k}) \end{bmatrix} = E(\mathbf{k}) \begin{bmatrix} \psi_A(\mathbf{k}) \\ \psi_B(\mathbf{k}) \end{bmatrix} = \mathbf{H}(\mathbf{k})\mathbf{\Psi}(\mathbf{k}) = \mathbf{E}(\mathbf{k})\mathbf{\Psi}(\mathbf{k})$$

Multiplying the first equation of the system for the second equation we get:

$$\gamma^2|f(\mathbf{k})|^2 = E^2(\mathbf{k}) \Rightarrow E(\mathbf{k}) = \pm\gamma|f(\mathbf{k})| \tag{1.6}$$

with $\gamma = 2.8eV$ hopping energy and where the upper sign is for the conduction (or π^*) band (electrons) and the lower sign is for valence (or π) band (holes).

The energy bands derived from the Hamiltonian have the form:

$$|f(\mathbf{k})| = \sqrt{(3 + 2cos(\sqrt{3}ak_x) + 4cos(\frac{3}{2}ak_y)cos(\frac{\sqrt{3}}{2}ak_x)} \tag{1.7}$$

which is symmetric around zero energy if $t' = 0$ (Figure 1.3). For finite values of t' the symmetry is broken and the bands become asymmetric. It is remarkable that at the corners of the first Brillouin zone, namely **K** and **K'**, the band is gapless, i.e. $E(\mathbf{K}) = E(\mathbf{K'}) = 0$.

Transport properties of graphene are around the Fermi level E_F so we need to examine the dispersion around the Dirac points. For this reason, we expand $f(\mathbf{K})$ in Taylor Series around **K** and **K'** as $\mathbf{k} = \mathbf{K} + \mathbf{q}$, with $|\mathbf{q}| \ll |\mathbf{K}|$: [4]

$$f(\mathbf{k}) = f(\mathbf{K}) + q_x\frac{\delta f(\mathbf{k})}{\delta k_x}|_{\mathbf{K}} + q_y\frac{\delta f(\mathbf{k})}{\delta k_x}|_{\mathbf{K}} + \cdots = f(\mathbf{K}) + q \bigtriangledown f(\mathbf{k})|_{\mathbf{K}} + \cdots \tag{1.8}$$

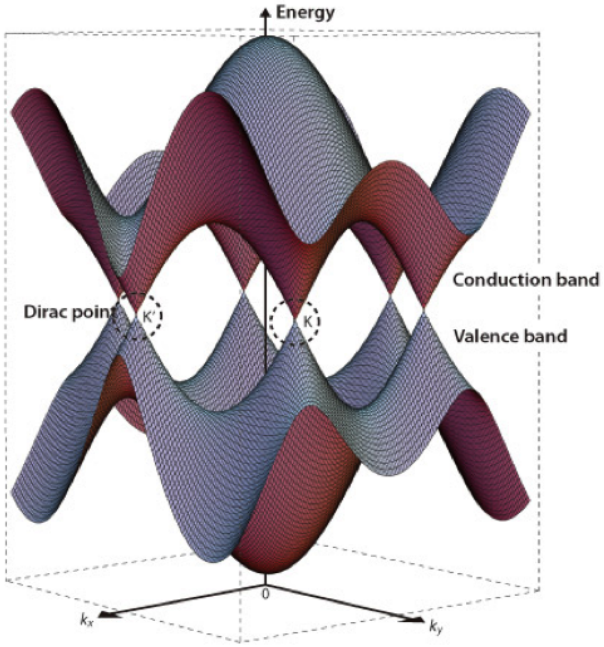

Figure 1.3: 3D representation of graphene bandstructure: valence band and conduction band meet in **K** and **K'**.

and the same around **K'**. At the end, we get:

$$f(\mathbf{k}) = \frac{3}{2}a(-q_x + jq_y) + \cdots \quad around \quad \mathbf{K} = (\frac{2\pi}{3a}, \frac{2\pi}{3\sqrt{3}a}) \tag{1.9}$$

$$f(\mathbf{k}) = \frac{3}{2}a(q_x + jq_y) + \cdots \quad around \quad \mathbf{K}' = (\frac{2\pi}{3a}, -\frac{2\pi}{3\sqrt{3}a}) \tag{1.10}$$

If we introduce these two function in the Hamiltonian definition (see above) we get:

$$\mathbf{H} = -j\frac{3}{2}a\gamma\sigma\bigtriangledown \tag{1.11}$$

which reminds the Dirac-Weyl Hamiltonian[1]:

$$\mathbf{H} = -jhc\sigma\bigtriangledown \tag{1.12}$$

describing the motion of massless relativistic particles. This leads us to the conclusion that around Dirac points, electrons and holes behave as massless Dirac fermions. We can approximate c to v_F and obtain for **K**:

$$\mathbf{H} = -jhv_F\sigma\bigtriangledown = hv_F\sigma\mathbf{q} = v_F\sigma\mathbf{p} \tag{1.13}$$

$$E(\mathbf{k}) = \pm\gamma|f(\mathbf{k})| = \pm\gamma\frac{3}{2}a|\mathbf{q}| = \pm v_F hq = \pm v_F p \tag{1.14}$$

$$\Psi(\mathbf{k}) = \frac{1}{\sqrt{2}}\begin{bmatrix} 1 \\ \pm\frac{f^*(\mathbf{k})}{|f(\mathbf{k})|} \end{bmatrix} = \frac{1}{\sqrt{2}}\begin{bmatrix} 1 \\ \pm\frac{q_x+jq_y}{|q_x+jq_y|} \end{bmatrix} = \frac{1}{\sqrt{2}}\begin{bmatrix} 1 \\ \pm e^{j\theta_q} \end{bmatrix} \tag{1.15}$$

while for **K'**[2]:

$$\mathbf{H}' = -jhv_F\sigma'\bigtriangledown = hv_F\sigma' q = v_F\sigma' \tag{1.16}$$

$$E(\mathbf{k}) = \pm\gamma|f(\mathbf{k})| = \pm\gamma\tfrac{3}{2}a|q| = \pm v_F hq = \pm v_F p \tag{1.17}$$

$$\Psi(\mathbf{k}) = \tfrac{1}{\sqrt{2}}\begin{bmatrix} 1 \\ \pm\frac{f^*(\mathbf{k})}{|f\mathbf{k}|} \end{bmatrix} = \tfrac{1}{\sqrt{2}}\begin{bmatrix} 1 \\ \pm\frac{q_x-jq_y}{|q_x-jq_y|} \end{bmatrix} = \tfrac{1}{\sqrt{2}}\begin{bmatrix} 1 \\ \pm e^{-j\theta_q} \end{bmatrix} \tag{1.18}$$

with v_F which is approximately:

[1] Actually the Schrödinger equation looks like the Dirac equation thanks to the symmetry of the crystal.

[2] In particular, we know that $(\sigma_x, \sigma_y)^* = (\sigma_x, -\sigma_y) \Rightarrow -(\sigma_x, -\sigma_y) = (-\sigma_x, \sigma_y) \Rightarrow \sigma' = -\sigma^*$.

$$v_F = \frac{3}{2}\frac{a\gamma}{h} \approx 10^6 m/s \approx \frac{c}{300}. \tag{1.19}$$

1.3 Hexagonal Boron Nitride

Boron nitride is a heat- and chemically-resistant refractory compound of boron and nitrogen with the chemical formula BN. It exists in various crystalline forms that are isoelectronic to a similarly structured carbon lattice.

The most stable crystalline form is the hexagonal one, also called h-BN, α-BN, g-BN, and graphitic boron nitride. Hexagonal boron nitride has a layered structure like graphite with boron and nitrogen atoms occupying the inequivalent A and B sub lattices in the Bernal structure (Figure 1.4). Within each layer, boron and nitrogen atoms are bound by strong covalent bonds, whereas the layers are held together by weak van der Waals forces [12]. Clearly, 2D hexagonal boron nitride has the same structure of graphene (Figure 1.2).

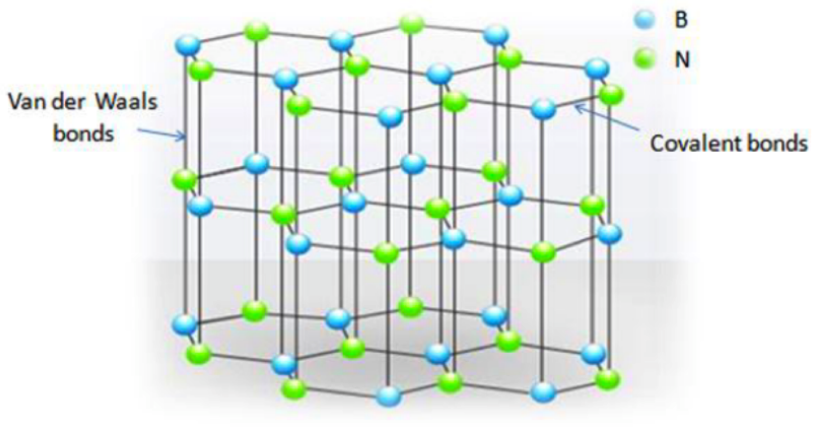

Figure 1.4: Layered structure of hexagonal boron nitride.

The different on-site energies of the boron and nitrogen atoms result in a large ($5.97eV$) bandgap [8] giving the h-BN property of good insulating material. The small (1.7%) lattice mismatch with graphite [10] and the owing to the strong, in-plane, covalent bonding of the planar hexagonal lattice structure, make the h-BN

relatively inert and expected to be free of dangling bonds or surface charge traps. Furthermore, the atomically flat surface can suppress rippling in graphene, which has been shown to mechanically conform to both corrugated and flat substrates. The dielectric properties of h-BN ($\epsilon \simeq 3 \div 4$ and $V_{breakdown} \sim 0.7 V nm^{-1}$) compare favourably with those of SiO_2, allowing the use of h-BN as an alternative gate dielectric with no loss of functionality [11]. All these features, make the h-BN a good material to improve graphene performances.

Chapter 2

Graphene electrical performances

In this chapter we will deal about some of the fundamental electrical properties of graphene. In particular we will talk about the very high theoretical mobility, about the intrinsic doping of the material and how is possible to measure it. Therefore, we will introduce the main features of a Graphene Field Effect Transistor (GFET), investigating which variables mostly influences graphene electrical performances.

2.1 Absence of Backscattering in Graphene

Equation (1.12) shows how electrons in graphene behaves as massless Dirac Fermions: this turns out in a very high value of carriers' v_F and, theoretically, a very high value of carriers mobility μ. What is more, considering a perfect 2D crystal, the probability associated to an event of backscattering in graphene is null. This result is extremely significative since backscattering is the main reason we have reduced mobility in a material. Indeed, transition (initial $\rightarrow$ final or $i \rightarrow f$) probability per unit time is given by Fermis golden rule [6]:

$$\frac{\delta P_{i\rightarrow f}}{\delta t} = \frac{2\pi}{h}\langle \mathbf{k_f}|H_{scatt}|\mathbf{k_f}\rangle^2 \rho_f \tag{2.1}$$

For charge carriers in graphene close to Dirac point which scatter at the impurity potential $V(r)$[1]:

[1]This formulation is only valid for long range potential.

$$\langle \mathbf{k_f}|H_{scatt}|\mathbf{k_f}\rangle \propto \int \langle \mathbf{k_f}, \mathbf{r}|H_{scatt}|\mathbf{k_f}, \mathbf{r}\rangle \tag{2.2}$$

where the free electron motion is given by a Bloch function:

$$|\mathbf{k_f}, \mathbf{r}\rangle = e^{j\mathbf{kr}}|\Psi(\mathbf{k}\rangle) \tag{2.3}$$

Therefore:

$$\langle \mathbf{k_f}, \mathbf{r}|H_{scatt}|\mathbf{k_f}, \mathbf{r}\rangle \propto \cos\frac{\theta_{qi} - \theta_{qf}}{2} \tag{2.4}$$

and since in a backscattering event $\theta_{qi} - \theta_{qf} = \pi$, it turns out that we have absence of backscattering close to the Dirac point.

2.2 Graphene Field Effect Transistor (GFET)

Considering a perfect graphene crystal, in which the mobility is infinite, is a strong approximation. In real crystals, we always have defects such that we can have scattering due to impurities or lattice vibrations and the mobility μ could reach high but not infinite values.

In addition, graphene properties are also strongly influenced by its immediate environment, including oxygen and any adsorbed molecules. Specifically, physisorbed molecules on graphene surfaces impact the electrical and thermal properties by doping or providing scattering sites, which effectively alter the electronic structure of graphene or reduce the mean free path of charge carriers or phonons. Resulting mobilities in the order of $1000 - 1500 cm^2 V^{-1} s^{-1}$ [9].

Indeed, when graphene is exposed to ambient, impurities act as dopants grabbing electrons from the valence band and pushing up the band-structure (Figure 2.1, up): practically, graphene becomes a p-type conductor. In this case, if we contact graphene with a drain and a source building a graphene resistor (Figure 2.1, down), we would have that $I_D = V_{DS}/R$ has a finite value, with R depending on carrier density and geometry factors.[2]

[2]Note that we are considering charges as uniformly distributed, otherwise we would have to look to $e - h$ puddles and thermal charges locally.

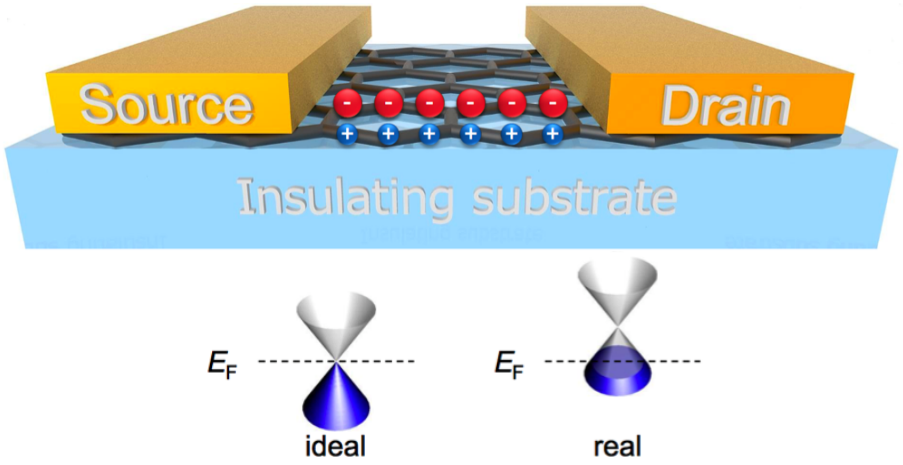

Figure 2.1: Up, graphene resistor made up with a graphene sheet and two contacts (drain and source); down, the bandstructure is pushed up due to p-doping induced by ambient impurities [6].

Now, let's assume we have a Graphene Field-Effect Transistor (GFET), made with a graphene resistor and three metal contacts (source, gate, drain) (Figure 2.2, up). Between gate and graphene there is an insulator as in typical semiconductor MOSFET. By changing V_{GS} we change carrier density in the channel, i.e. we control the channel resistance R. If the graphene resistor has a natural amount of positive charge Q_P coming from the environment doping, when we act on V_{GS} we have a net amount of charge in the channel given by [6]:

$$Q = Q_P - Q_G = Q_P - C_G V_{GS} \tag{2.5}$$

where C_G is the capacity of the capacitor of the GFET. Thus, the band-structure moves down and the channel becomes less conductive.

The bottom part of Figure 2.2 shows the transfer voltage characteristic of GFET for small V_{DS}. When $V_{DS} = 0$ it is the case of a graphene resistor. As V_{GS} increases and we attract electrons, R also increases and the E_F gets closer to the Dirac point. When V_{GS} reaches a threshold value of V_{th}, the number of induced charges Q_G is equal to Q_P and the current reaches the minimum value: for $T = 0K$ we would have $I_D = 0$ but thanks to the thermal excitations and puddles the value is different from 0. From this value of V_{GS} the band-structure keeps moving down and we start to conduct with electrons: the channel has been inverted.

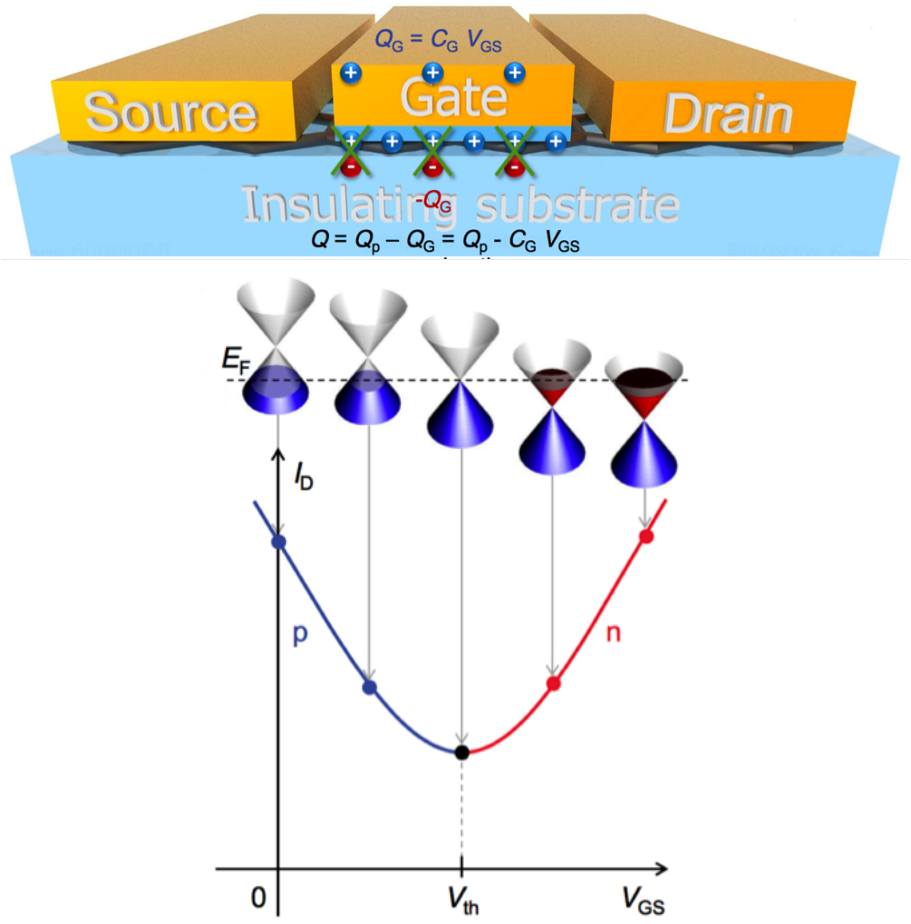

Figure 2.2: *Up*, the transfer voltage characteristic of a GFET: as V_{GS} increases, the bandstructure is pushed down. At V_{th} the channel is inverted and we conduct with electrons; *down*, graphene field effect transistor (GFET) made up adding a gate contact to a graphene resistor [6].

However, it is better to remark that this ambipolar behaviour of the transfer voltage characteristic is not symmetric respect to the minimum ($V_{GS} = V_{th}$). As known, the hole mobility is such that $\mu_h = 3\mu_e$ and we also have scattering due to positive charged traps in the channel which attract electrons (negative) and repels holes (positive). Thus, for a certain value of $\overline{V_{GS}}$ such that $|\overline{V_{GS}} - V_{th}|$ represents the distance from the minimum $V_(th)$ both in the p and n regimes, we will always have that $I_{D_n} < I_{D_p}$.

2.3 Transfer Voltage Characteristic of GFET

If we apply a larger (positive) V_{DS}, things inside the channel of a GFET changes. Now V_S differs from V_D. If graphene were a ballistic conductor (no scattering centers) we would have a potential distribution such that potential drop will be in correspondence of metal contacts, where charge carriers thermalize with source and drain. However, in real situations, we could treat graphene as a conventional resistor between S and D diffusive transport material in which the voltage distribution is linear among the channel following Ohm's law. In this case, being L the length of the channel and x a generic point of the channel, the potential between the gate and the channel goes like [6]:

$$V_{Gch}(x) = V_G - V_{ch} = V_G - V_S - \frac{x}{L}V_{DS} \tag{2.6}$$

and since we have a lowering V_{ch}, as we approach the drain contact, we have less negative induced charges. In particular, the charge density in the channel goes like:

$$\sigma(x) = \sigma_p(x) - \sigma_G(x) = C_{ox}V_{th} - C_{ox}V_{Gch}(x) \tag{2.7}$$

Figure 2.3 shows how the transfer characteristic of the GFET changes.

When V_{GS} is null, we have an increase of the current for the extra holes in the channel which is now more conductive. When $V_{GS} = V_{th}$ the curve hasn't reached the minimum yet, because of the extra holes. A further increase of V_{GS} produces electron on the S side of the GFET and the minimum falls where:

$$V_{Gch}\frac{L}{2} = V_{th} = V_{GS} - V_{DS_2} \tag{2.8}$$

From this value of V_{GS} we mainly start to conduct with electron and the I_D/V_{DS} curve raises again.[3]

[3]Again, not only the transfer voltage characteristic is not symmetric respect to the minimum, but it slightly moves up.

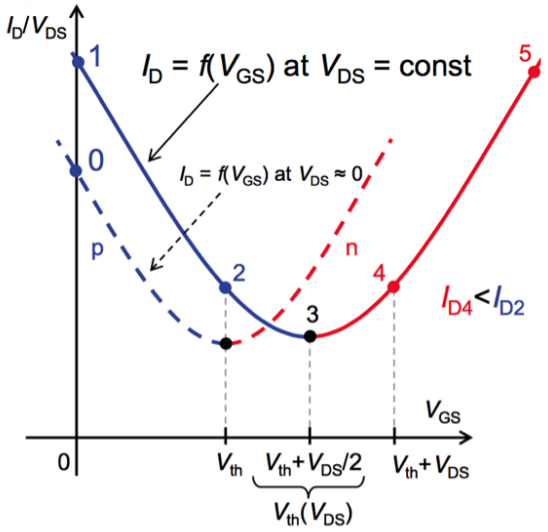

Figure 2.3: Comparison between transfer voltage characteristics of a GFET at $V_{DS} \approx 0$ (dashed curve) and $V_{DS} = const$ (full line). The curve at $V_{DS} = const$ is shifted to the right due to the applied V_{DS} which forces the potential along the channel to follow Ohm's Law [6].

2.4 Graphene based electrical devices

The fabrication and the characterization of graphene-based electrical devices requires the transfer of graphene from the catalyst onto appropriate substrates such as SiO_2/Si, Si_3N_4, etc.. The transfer can be carried out through a wet [13] or dry [14] process. Currently, the most common transfer methods on large areas rely on sacrificial polymer layers deposited on top of the graphene or h-BN (for example PMMA, polystyrene [15], polybutadiene [16]) to provide mechanical support during the wet etching of the catalyst. However, polymer residues that lie behind due to incomplete removal of the support layer are the dominant source of extrinsic doping reported in CVD graphene devices [17] and, as we saw in previous sections, could strongly alter graphene performances. Transfer process is also a critical part that needs to keep both graphene and h-BN free of defects.

The enhancement of the physical and electrical properties of graphene grown by CVD via controlling the effects of polymer residues have been widely studied [18]. Pirkle et al. [19], demonstrated that residual PMMA clearly plays a significant role in *p*-type chemical doping of transferred CVD graphene, while trapped species

(as water) at the graphene/substrate interface should be considered. Recently, researchers have focused on the possibility to deposit an activation layer onto the target substrate in order to avoid the graphene to suffer the effects of strain, roughness and minimize hydrophobicity issues when transferred onto a target substrate. Several materials have been selected as candidates for activation layers between the substrate and the graphene: Self-Assembled Monolayers, better known as SAMs, like perfluorodecyltrichlorosilane (FDTS), highly oriented pyrolytic graphite (HOPG), hexamethyldisilazane (HMDS), and others like Teflon, parylene-C and last but not least hexagonal boron nitride (h-BN). On the other hand, the effect of dopants coming from the environment and polymers used during transfer and post-processing could be avoided by using an encapsulation layer which protects the graphene. Aside from aluminum oxide (Al_2O_3), h-BN has also been selected as a good encapsulating material. In this sense, h-BN seems the most promising material for high electrical performance applications in graphene electronics.

2.5 Mobility state of the art

Recently, Banszerus et al., reported an advanced delamination and encapsulation method that overcomes these problems and results in CVD-grown graphene devices with properties comparable to those of high-quality exfoliated graphene [21]. This method relies on strong Van der Waals interactions between the graphene and the h-BN, which allow to pick-up graphene directly from copper and encapsulate it in h-BN avoiding any polymer contamination at the h-BN/graphene interface. In brief, the method consists in covering a polymer stack consisting of polydimethylsiloxane (PDMS), polyvinylalcohol (PVA) and polymethylmethacrylate (PMMA) with an exfoliated h-BN flake, and using it to pick-up a small area of CVD graphene directly from its growth substrate. The whole structure is further transferred onto another substrate, such as exfoliated h-BN itself (Figure 2.4).

With this method, all the investigated devices exhibit an extremely narrow Raman 2D peak with full width at half maximum (FWHM) of the 2D peak about $20cm^{-1}$ and a very high mobility up to 320,000$cm^2V^{-1}s^{-1}$ and 350,000$cm^2V^{-1}s^{-1}$ for electrons and holes respectively at T=1.6K and a value of 50,000$cm^2V^{-1}s^{-1}$ at room temperature. Whats more, the doping level has been demonstrated to be $n = 5 \cdot 10^{11}cm^{-2}$.

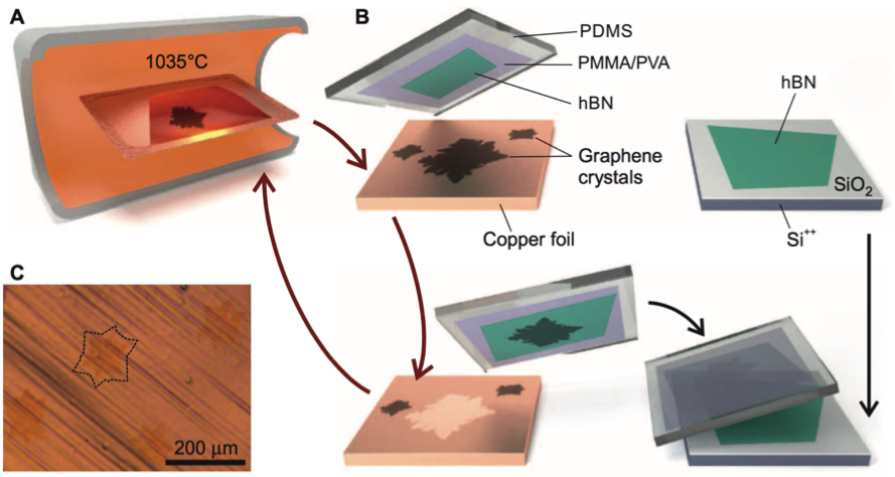

Figure 2.4: Dry transfer of CVD-grown graphene. (A) Illustration of the CVD furnace with a copper enclosure inside. (B) Process schematic of the contamination-free transfer of CVD graphene from copper onto hBN. (C) Optical microscopy image of grown graphene crystals on copper foil [21].

At the same time, measurements on CVD graphene properties with CVD multilayer h-BN as dielectric material has been performed. Kim et al. [20] created an heterostructure depositing a $15nm$ thick h-BN film on top of a $300nm$ SiO_2/Si substrate and further depositing a large-area (hundreds of microns) single crystalline CVD-grown graphene on the top of the h-BN film. At room temperature, the carrier mobility exceeds over $10{,}000cm^2V^{-1}s^{-1}$ with a peak value of $24{,}000cm^2V^{-1}s^{-1}$. The large distribution of values might be related more to the quality of the graphene transfer rather than the variations of the material quality of both h-BN and graphene, showing that the quality of the transfer plays an important role in the graphene electrical performances.

Chapter 3

How do we get atomically thin materials?

Nowadays, there are many different approaches to get atomically-thin layers of a given materials. In this work we will focus on two of them: mechanical exfoliation and chemical vapor deposition. Mechanical exfoliation by scotch tape was the first method ever used by Andre Geim and Konstantin Novoselov in order to isolate graphene [1]. Furthermore, the method was extended to h-BN. The strong in-plane bonding of both graphene and h-BN, which provides their stability, and the weak out-of-plane van der Waals interactions, caused by correlations in the fluctuating polarizations of nearby particles because of quantum dynamics, allow the cleavage of the material onto two-dimensional (2D) layers. So far, this technique has given the most relevant results in terms of electronic properties even though only limited micrometer sized samples can be prepared. Thus, the Chemical Vapor Deposition method (CVD) onto specific substrates was introduced and the possibility to grow large area thin films is nowadays a reality.

3.1 CVD graphene

The most promising and readily accessible approach for deposition of reasonably high quality graphene is Chemical Vapor Deposition (CVD) onto transition metal substrates such Ni, Pd, Ru, Ir or Cu [22]. In this work, we will use graphene grown on copper foil. Indeed, the use of copper as catalyst is one of the methods for producing continuous monolayer of high quality graphene over large areas. The mechanism is surface related due to the peculiar interactions between Cu and C and

self-limited to a single layer of graphene [22] thanks to the low solubility of carbon in copper. The monolayer growth on Cu is easier to control than using for example Ni. In this work we will use one of the standard GRAPHENEA recipes.

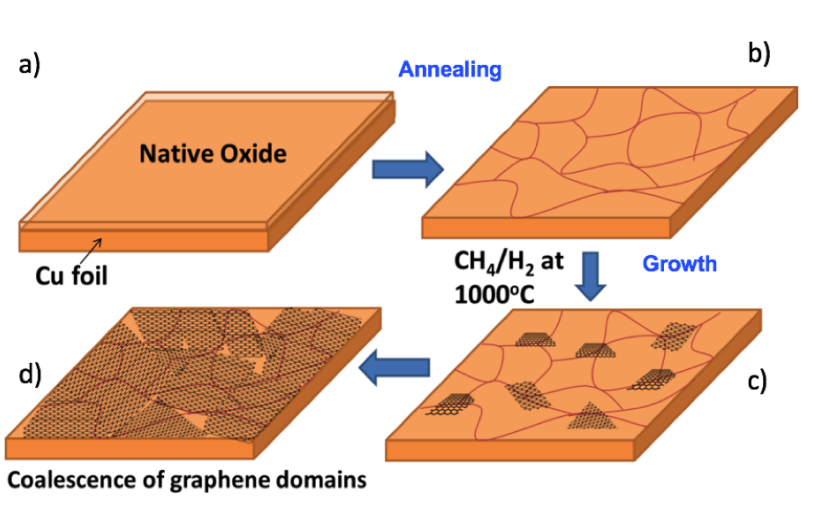

Figure 3.1: Schematic illustration of the four main stages of graphene growth on copper by CVD: (a) copper foil with native oxide; (b) the annealing of the copper foil at 1000°C under a mixture of H_2 and Ar flow; the exposure of the copper foil to $Ar/H_2/CH_4$ at 1000°C leading to the nucleation of graphene islands; (d) enlargement of the graphene flakes with different lattice orientations. [22]

Prior to introducing the $25\mu m$ thickness Alpha Aesar Cu foil in the CVD system, a chemical surface pre-treatment with an acid solution (HNO_3 or Acetic Acid) is carried out in order to remove the native copper oxide and other impurities (Figure 3.1 a). The pre-treatment of the copper foil has been found to be important in obtaining large graphene domains in the as-deposited product [24] [23] and serves several important functions that ensure high quality graphene deposition like improving the flatness of the copper and decreasing the multilayer areas formation (Figure 3.1 b). Once the copper is clean, it is placed in the reactor chamber. The graphene synthesis was carried out using a cold walled CVD reactor (Aixtron BM [37]) at low pressure using methane as carbon source. Prior to the growth, the Cu foils were annealed at 1000°C under a mixture of H_2 and Ar flow in order to further clean the Cu surface from the oxide and increase its grain size. Once the catalyst surface is ready methane is introduced in the chamber. The growth is performed at around 1000°C, very close to the melting temperature of the Cu, for 10 min using a mixture of $Ar/H_2/CH_4$ (Figure 3.1 c, d). Once the film is complete the system is

cooled down. The result is a complete graphene film on both sides of the copper. The bottom layer is typically removed.

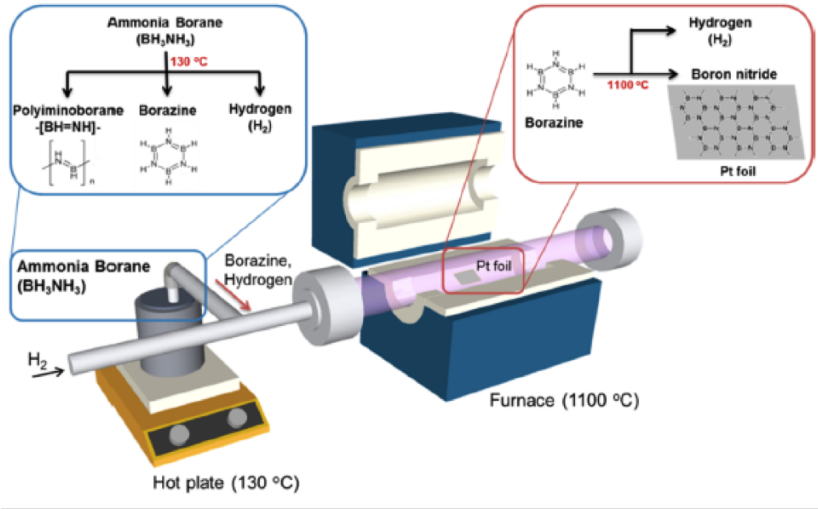

Figure 3.2: Schematic setup of the h-BN growth by CVD for platinum substrate.

3.2 CVD Hexagonal Boron Nitride

Song et altri reported the large area synthesis on copper of multilayer h-BN films consisting of two to five atomic layers using atmospheric pressure chemical vapor deposition (APCVD) [12]. Figure 3.2 shows a schematic setup of the process for platinum substrate but the same scheme holds for copper. The synthesis of h-BN films was carried out in a split tube furnace with a fused quartz processing tube ($50mm$ outside diameter). A copper foil with $25\mu m$ thickness was used as substrate. As for graphene, the Cu foil was pretreated in order to remove impurities and native copper oxide by washing with diluted nitric acid and deionized water. Then it was placed in the center of a furnace, annealed at 600°C for 20 min in Ar/H_2 (15 vol % H_2, 85 vol % Ar) flow at $500sccm$. The furnace was then gradually heated up to 1000°C in 40 min. Ammonia borane (NH_3-BH_3) was sublimated at $120 - 130$°C by using a heating belt and then carried into the reaction region by Ar/H_2 gas glow. During the growth process, Ar/H_2 flow was kept at $200sccm$. The typical growth time is 30-60 min. After growth, the furnace was quickly cooled down to room temperature. HRTEM images and Fast Fourier Transform (FFT) (Figure 3.3)

confirm that the film is formed by (mainly) 2 hexagonal patterned layers with some regions up to 5 layers.

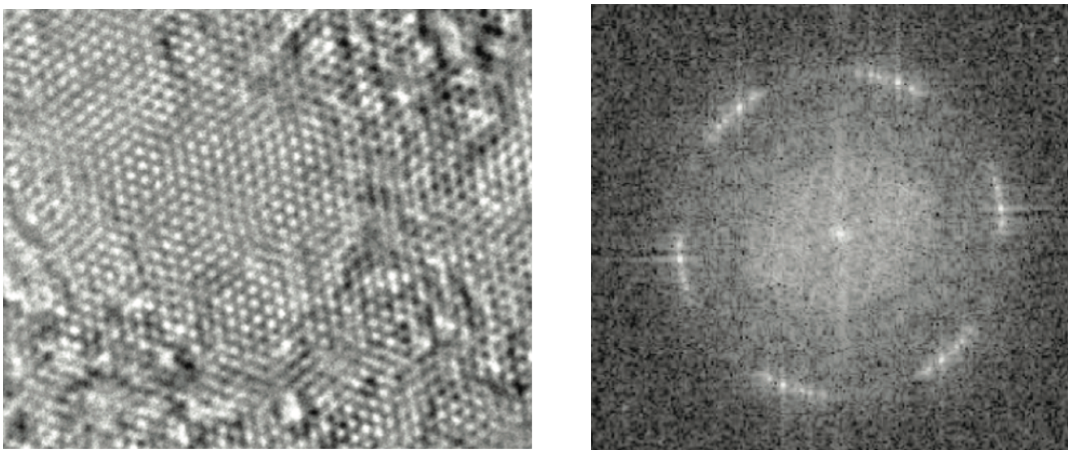

Figure 3.3: A typical atomic image of a h-BN films. The scale bars is 2 nm (left); the FFT pattern, which indicates a five-layer stacked region (right) [12].

Regarding lower thickness, monolayer h-BN single crystals have been successfully synthesized by ultra-high vacuum chemical vapor deposition (UHVCVD) on single-crystal noble and transition metals such as Ru, Rh, Rt, Pt, Ni, Pd, Ag, and Cu. What is more, inspired by the recent progress of graphene synthesis, the growth of wide area h-BN has been investigated with various polycrystalline metals such as Ni, Co, Pt, and Cu using LPCVD or atmospheric pressure chemical vapor deposition (APCVD) [25]. Compared to the LPCVD approach, the APCVD holds the benefit of lower cost and better safety but first reports expressed concern about APCVD being uncontrollable for the monolayer h-BN synthesis. However, Stehle et al. recently presented a work in which they could grow large area h-BN Monolayer up to 2x2" using ammonia borane as precursor and $125\mu m$ copper foil as substrate in APCVD environment.

Kong et al. reported for the first time the growth of good quality large area monolayer h-BN on Cu foil with h-BN synthesis under low pressure (LPCVD). With this pressure conditions, the growth is preferentially surface reaction limited and the results are less affected by the geometry of the substrate or gas flow effect [27].

Figure 3.4 shows a schematic diagram of the LPCVD setup. To synthesize the monolayer h-BN on Cu foil ($25\mu m$ Alpha Aesar) using LPCVD, ammonia-borane was used as precursor and it was heated up to 90°C in a ZrO_2 boat inside a small

quartz tube (heating zone 1) to prevent it from flowing away during vacuum pumping. The furnace (heating zone 2) is heated up to 1000°C and the copper foil is annealed under $10sccm$ H_2. As for graphene, the annealing of Cu has been found to be crucial to obtain large sized h-BN triangular-shaped single crystals: for instance, Song et al. reported the growth of h-BN with a domain size up to $72\mu m$ pre-annealing the Cu foil at least for 6 hours [26] (Figure 3.6(left)).

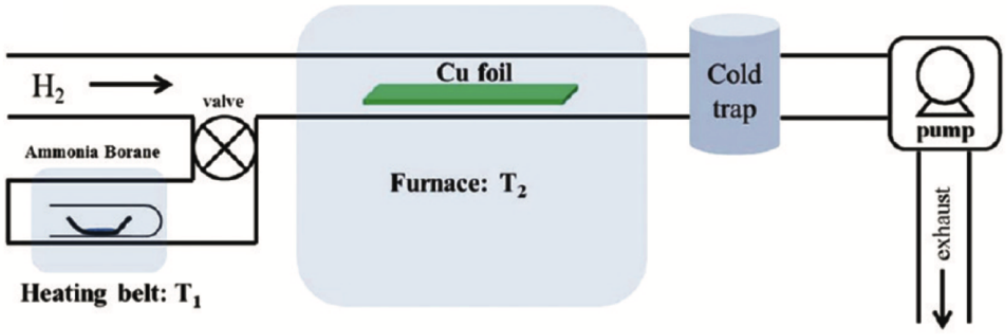

Figure 3.4: The schematic diagram of hexagonal boron nitride (h-BN) LPCVD synthesis setup, T_2 temperature is fixed at 1000°C for this study [27].

Then growths with same conditions have been performed for 10, 15, 40, 60, and 120 min of growth time. Comparing the 10 min (Figure 3.5a) growth result with the 15 min (Figure 3.5b) result, it appears that the initial flakes are increased both in size (area) and density (i.e., more nucleation sites come out) for longer growth times. Both the triangular shape and the asymmetric diamond shape were observed as the initial form of the flakes. h-BN flakes growing across Cu grain boundaries were also observed frequently. A similar observation has been reported for graphene growth on Cu foil. This suggests that h-BN growth in LPCVD is surface-mediated. By 40 min (Figure 3.5c) the monolayer growth is almost complete and an open Cu surface can hardly be found under SEM. On the other hand, characteristic wrinkles are observed on the surface.

Furthermore, sites with multiple layers appear, as outlined by the red triangles (Figure 3.5f). With even longer growth periods (60 and 120 min), these multilayer sites increase in density (Figures 3.5d and 3.5e). After 120 min growth, the surface was mostly covered by multilayers of triangles.

Regarding the triangular shape of the flakes, (Figure 3.6 (right)) illustrates a nitrogen-terminated triangular island. It turns out that the next triangle must be a

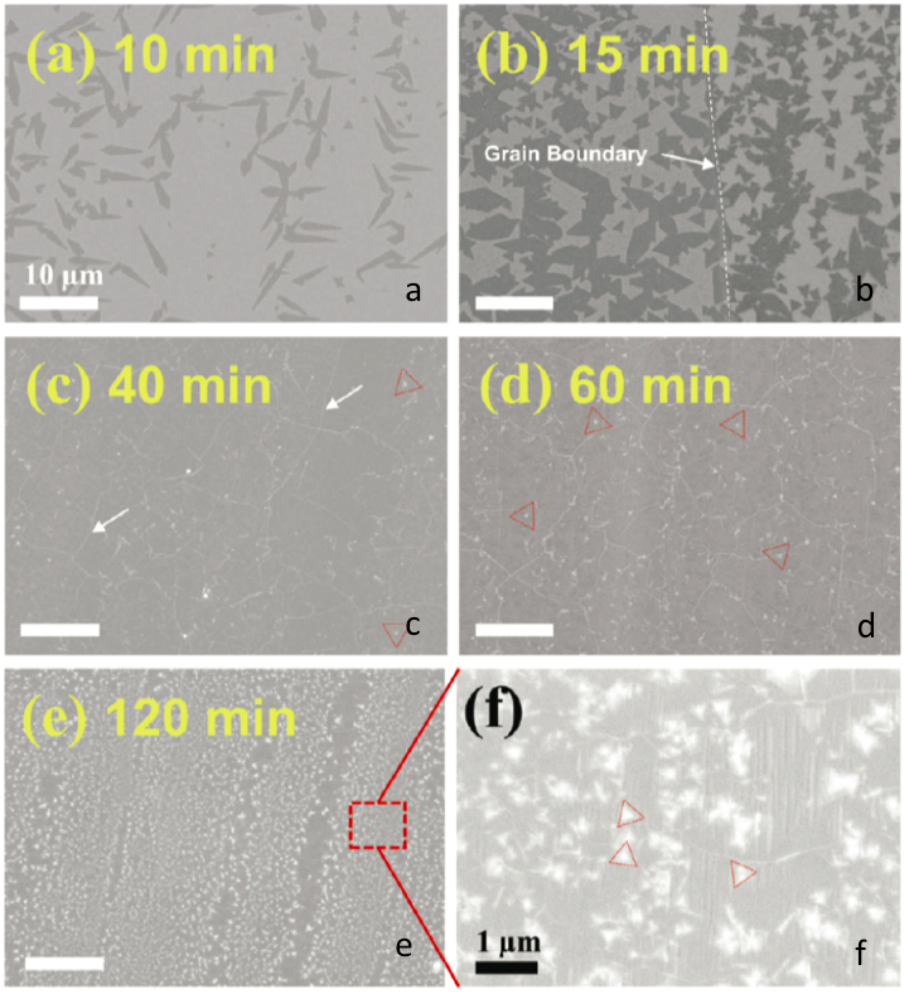

Figure 3.5: Growth time dependence with $T_1 = 70°C$. SEM images of (a) 10, (b) 15, (c) 40, (d) 60, and (e) 120 min in growth time, respectively. (f) Higher magnification of the dotted square region in (e). The dotted red triangles indicate the multilayered h-BN region [27].

boron-terminated triangle from simple geometry, and if a hexagonal flake of h-BN is formed by this way, the edges need to be nitrogen-terminated and boron-terminated alternating with each other. However, this would be energetically unfavorable as boron-terminated edge will cost more energy. Therefore, this suggests why h-BN flakes are triangular-shaped instead of hexagonal. In fact, the growth of hexagonal flakes of h-BN has never been observed or reported in the literature [27].

In good-quality h-BN growth, two different precursors (solid and liquid) have been used: ammonia-borane (BH_3-NH_3, also called borazane) or borazine ($B_3N_3H_6$),

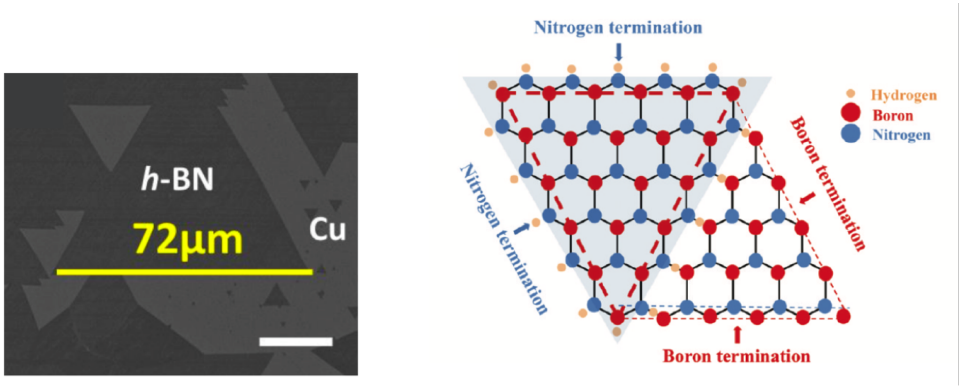

Figure 3.6: SEM image of large domain h-BN triangle showing the edge length of $\approx 72\mu m$. Scale bar: $20\mu m$ (left). [26]; schematic illustration of a nitrogen-terminated h- BN triangle, the triangle next to it can only have boron-termination at the edges (right). [27]

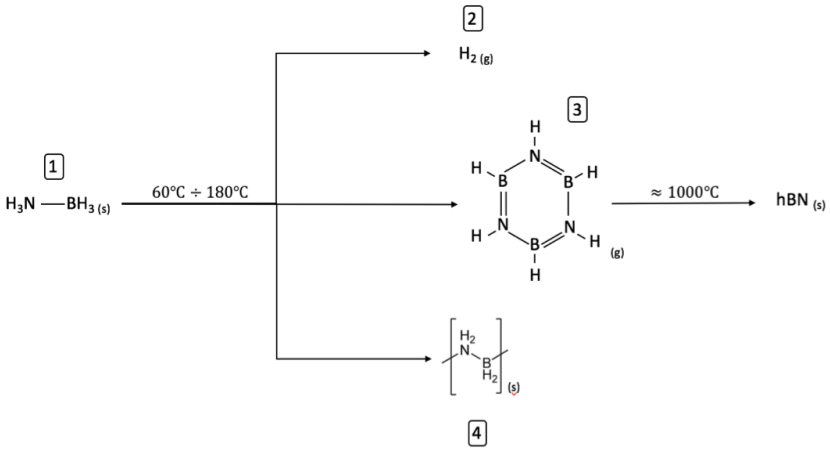

Figure 3.7: Experimentally observed chemical pathways in the pyrolytic decomposition of ammonia borane to boron nitride. [1] Ammonia Borane; [2] hydrogen H_2; [3] borazine; [4] polyaminoborane (PAB); finally, borazine undergoes a dehydrogenation reaction at very high T and forms hexagonal boron nitride (h-BN).

both having a 1:1 B:N stoichiometry. However, the growth mechanism still remains uncertain. Ammonia-borane is usually preferred as the precursor instead of borazine because of its stability in ambient, wider availability and cheaper price (in contrast, borazine is moisture-sensitive and hydrolyzes to boric acid, ammonia and hydrogen). High-purity ammonia-borane shows no decomposition over two months at room temperature and its vapor pressure is estimated to be 10^{-4}Torr at room temperature [28].

Ammonia borane is a molecular solid currently being investigated as a chemical hydrogen storage material because of its high hydrogen content (19.6 wt%) and favorable hydrogen release characteristics [29]. The molecule (1) adopts a structure like ethane, which is isoelectronic. The B-N distance is 1.58$\mathring{A}$. The B-H and N-H distances are 1.15$\mathring{A}$ and 0.96$\mathring{A}$, respectively. BH_3-NH_3 firstly decomposes into hydrogen (H_2; gas) (2), polyiminoborane (BH_2-NH_2; solid) (4), and borazine ($B_3N_3H_6$; gas) (3) during a wide temperature range of 60-180°C. The main reactant borazine undergoes dehydrogenation reaction, transforming into poly-BN-rings and finally produce h-BN layer under high temperature (Figure 3.7).

Chapter 4

Transfer and Characterization of CVD films

So far, from the first-time graphene was isolated, many techniques have been developed in order to characterize it. In this section, we introduce several characterization methods in order to characterize both the graphene and the h-BN. Optical characterization, Raman Spectroscopy and Atomic Force Microscopy (AFM) are characterization techniques providing morphology and structural information showing how is the quality of the thin layer in terms of impurities and defects. In addition, Transmission Electron Microscopy (TEM) will be used to identify the real spatial distribution of the atoms and that allows the verification of the hexagonal structure of both materials. XPS and IR spectroscopy are used in order to get information about the constituents of the material, i.e. carbon, boron and nitrogen. However, since the characterization method requires the 2D film to be transferred from the catalyst onto a more suitable rigid substrate, we now first describe in details the assisted PMMA wet transfer process for thin film materials which allows us to transfer both graphene and h-BN to a $300nm$ SiO_2/Si substrate.

4.1 Standard assisted PMMA wet transfer process

We will use 1x1 cm^2 squares grown on copper foil as samples for the transfer. Figure 4.1 refers to graphene transfer steps but is also valid for h-BN:

1. Spin-coating of the sample with $495A2$ PMMA at $\approx$ 2500 rpm for 75 seconds

(Figure 4.1b).

2. Bottom layer removal through Reactive-Ion Etching (RIE) with O_2 plasma ($20sccm$) for 10 seconds at 100W power (pressure 5 Pa) (Figure 4.1c).

3. Copper etching in $FeCl_3$ etchant solution for 40 minutes (Figure 4.1d).

4. Cleaning of the film from any etchant contamination during 10 min in each solution: H_2O/HCl (10%wt)/ H_2O/H_2O.

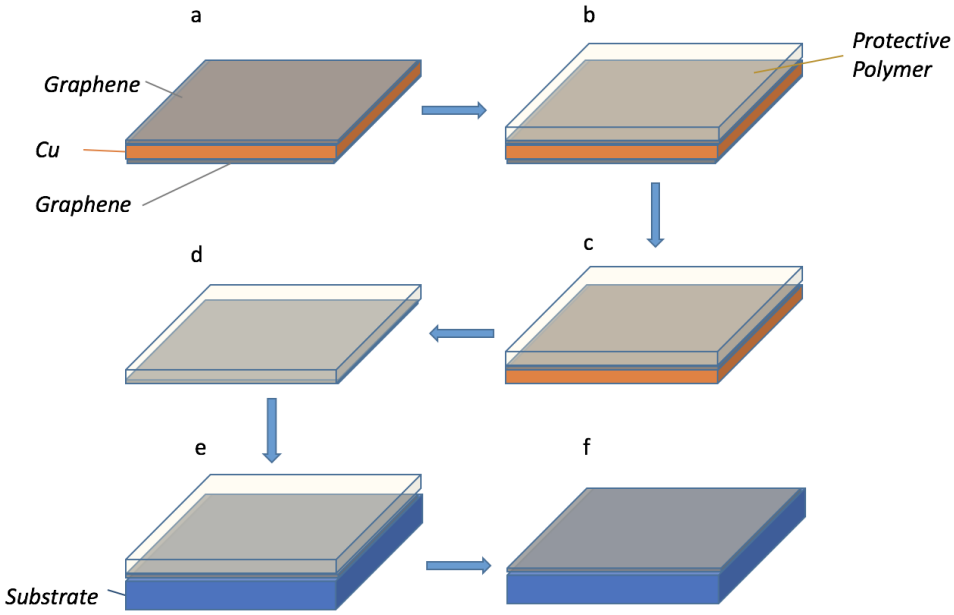

Figure 4.1: Standard assisted PMMA wet transfer process: a) Cu substrate covered on both sides with graphene; b) spincoating of the PMMA on the top (good) layer; c) bottom layer removal throughout plasma RIE; d) copper etching in $FeCl_3$ etchant solution; e) scooping of the sample with the substrate; f) PMMA removal with solvents.

Finally, we deposit the PMMA/2D Material onto a clean 300nm SiO_2/Si substrate (SiLTronix [30]) (Figure 4.1e); this "scooping" operation is important because we must avoid trapped water between the substrate and the film, representing one of the most common dopants and decreasing the electrical properties of graphene. Nevertheless, to fully remove water is difficult: thus, to get rid of it as much as possible we let the sample dry over night at 60°C in vacuum and further applying an additional drying step up to 180°C. Once the sample is dried, we use solvents to remove PMMA (Figure 4.1f) from the film by dipping into:

1. Acetone (30 min) to remove PMMA layer.

2. Isopropanol (30 min) to clean Acetone and residues from the sample.

We let the sample dry on a hot plate at $\approx 120°C$ for several minutes to let the IPA evaporate. The result of a transfer process is shown in Figure 4.2.

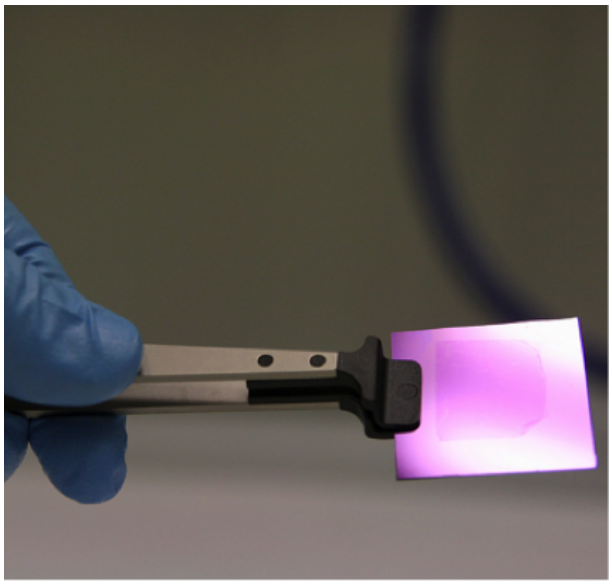

Figure 4.2: Standard assisted PMMA wet transfer process final result: as we can observe, graphene is eye-visible.

4.2 Optical Microscopy Characterization

The optical characterization is the easiest and fastest way to obtain a first quality control of the 2D material after growth on the Cu foil catalyst and onto $300nm$ SiO_2/Si. Thin film or even flakes of graphene are sufficiently transparent to add an optical path, which changes their interference color with respect to an empty wafer [1]. For a certain thickness of SiO_2 even a single layer was found to give sufficient, albeit feeble, contrast to allow the huge image processing power of the human brain to spot a few micron-sized graphene crystallites among copious thicker flakes scattered over a mm-sized area [31]. Instead, because of its zero opacity (the band gap is larger than 5eV), atomically-thin BN exhibits little optical contrast, even if the interference enhancement using oxidized Si wafers is employed. For the standard

oxide thickness of $300nm$ SiO_2, h-BN Monolayers show a white-light contrast of $< 1.5\%$, which make them almost undetectable by the human eye. Moreover, the contrast changes from positive to negative (BN is darker than the substrate at long wavelengths and brighter at short ones) when crossing from the red to the blue parts of the spectrum, going through zero in the green region where the eye sensitivity is at a maximum [32]. Nevertheless, the contrast increases proportionally as the number of layers increases: for this reason, the h-BN MultiLayer sample shows an extremely higher contrast than h-BN MonoLayer, which makes it easily detectable by the human eye. Optical characterization was performed with a Nikon Eclipse LV100 microscope connected to a Nikon DS-Fi2. Samples are placed on a sliding stage (PRIOR) controlled with a sensible joystick (PRIOR). Pictures are taken at different magnifications (5x, 20x, 50x, 100x) each showing more details of the films.

4.3 Raman spectroscopy

Crossing the optical results with the Raman characterization we can extract more information regarding the structural quality of the transferred films, graphene and h-BN, onto $300nm$ SiO_2/Si. The system used was Confocal Raman Spectroscopy from WiTec [38] using a green Nd: YAG laser ($\lambda = 532nm$). The objective is fixed at 100x magnification such that the scanned area is $1\mu m^2$. After a first calibration of the system, the sample is placed on a x, y, z stage and both its position and the focus are controlled with a micro-manipulator while the power of the laser must be set $<$ 1mW in order not to burn the 2D film. Center wavelength is set at $630nm$.

4.4 IR spectroscopy

The IR measurement is another nondestructive method using vibrational modes for printing a material. In this work, we will use IR spectroscopy in order to characterize only h-BN after growth and transferred onto $300nm$ SiO_2/Si. Measurements were performed in reflection mode (HYPERION microscope, Vertex 70 spectrometer [39]) since the SiO_2 is not transparent to the IR signal. Acquisition range is from $2000cm^{-1}$ to $80cm^{-1}$ (complete mid and far IR spectrum) and in order to get a well-defined spectrum a background SiO_2 spectrum is used for normalization. Both background SiO_2 and CVD h-BN spectra are acquired with 250 scans and $4cm^{-1}$ of resolution.

4.5 Atomic Force Microscopy

We will also use Atomic Force Microscopy (AFM) in order to characterize both graphene and h-BN: in particular, we will use AFM to determine the thickness of the layer on samples transferred onto $300nm$ SiO_2/Si. It has a demonstrated resolution of the order of fractions of a nanometer, more than 1000 times better than the optical diffraction limit. The AFM instrument we used is from Agilent Technologies [40].

4.6 X-Ray Photoemission Spectroscopy

In Section 5.2 regarding the synthesis of the hBN, we will use X-Ray Photoemission Spectroscopy (XPS) to characterize the obtained film. XPS experiments were performed in a SPECS Sage HR 100 spectrometer [41] with a non-monochromatic X-ray source of Magnesium with a Kα line of $1253.6eV$ energy and 250W. The samples were placed perpendicular to the analyzer axis and calibrated using the $3d^{\frac{5}{2}} = 368.27eV$ line of Ag with a full width at half maximum (FWHM) of $1.1eV$. An electron flood gun was used to compensate for charging during XPS data acquisition. The selected resolution was $30eV$ and 15eV of Pass Energy and $0.5eV$/step and 0.15eV/step for the survey and high resolution spectra, respectively. Measurements were made in an ultra-high vacuum (UHV) chamber. For our data, the Shirley-type background subtraction was used and all curves were defined as 40% Lorentzian and 60% Gaussian.

4.7 Transmission Electron Microscopy

In order to obtain HR-TEM images, the monolayer graphene was transferred onto Quantifoil TEM Grids with $2\mu m$ holes where graphene and hBN are freestanding. The 2D films images are taken in high resolution. TEM mode at $80kV$ in a Titan G2 60-300 with image Cs-corrector is used.

4.8 Characterization of CVD commercial Monolayer graphene

In this work we have used one of the standard commercial materials produced by GRAPHENEA, graphene grown on Cu foil catalyst. Pieces of 1x1cm^2 have been transferred by the above described wet transfer process in order to characterize the material. In Figure 4.3 (left), both low and high magnification images show that the Monolayer graphene film is clean, free of holes and cracks meaning that the transfer quality is very good. The presence of wrinkles is due to the growth process where the difference in the thermal expansion coefficient between Cu ($24 \cdot 10^{-6} K^{-1}$) and graphene ($6 \cdot 10^{-6} K^{-1}$) is responsible of difference rate of expansion and contraction. At high magnification, some multilayer regions of $\approx 1 \mu m^2$ size can be observed.

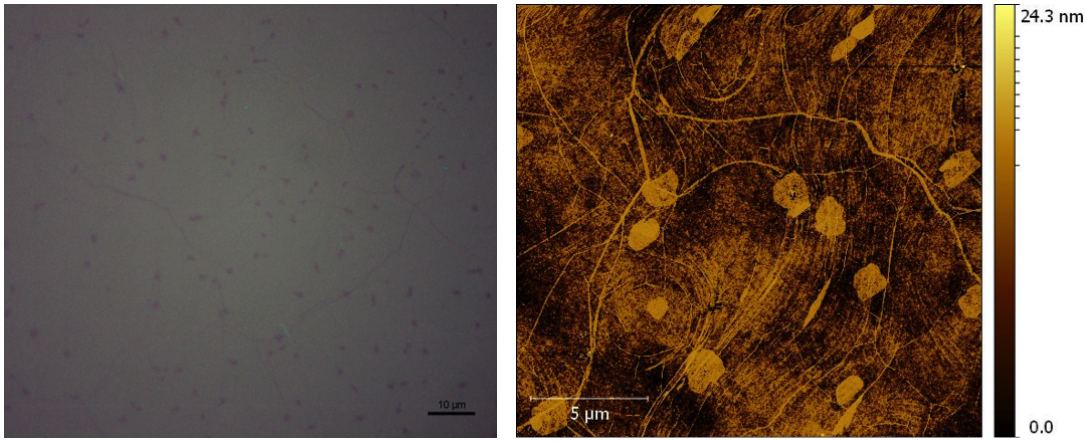

Figure 4.3: Optical image (100x) of a single layer of graphene: dark spots are multilayer regions (left); scanned area with AFM of the sample on the left: the contrast reveals the presence of some multilayer regions (right).

Further analysis of the same sample with an AFM (Figure 4.3, right) revealed that they are mainly bilayers. Multilayers are usually formed due to defects and impurities present on Cu. We measured the area of multilayers resulting in below 5% of the total area of the film. Raman results are shown in Figure 4.4. Measurements are usually performed setting 5s integration time and 5 accumulations for graphene. What we find in a graphene Raman spectrum, is the presence of 3 peaks:

1. The D peak at $\approx 1350 cm^{-1}$, which indicates the amount of disorder in carbon materials and increases with the number of structural defects.

2. The G peak at $\approx 1580 cm^{-1}$, due to the doubly degenerate zone center E_{2g} mode; typically, this peak is symmetric except in regions containing wrinkles or grain boundaries and the shape and the intensity are strongly influenced by the number of dopants in the material.

3. The 2D (or historically G') peak $\approx 2700 cm^{-1}$, due to the second order of zone boundary phonons, gives the number of layers.

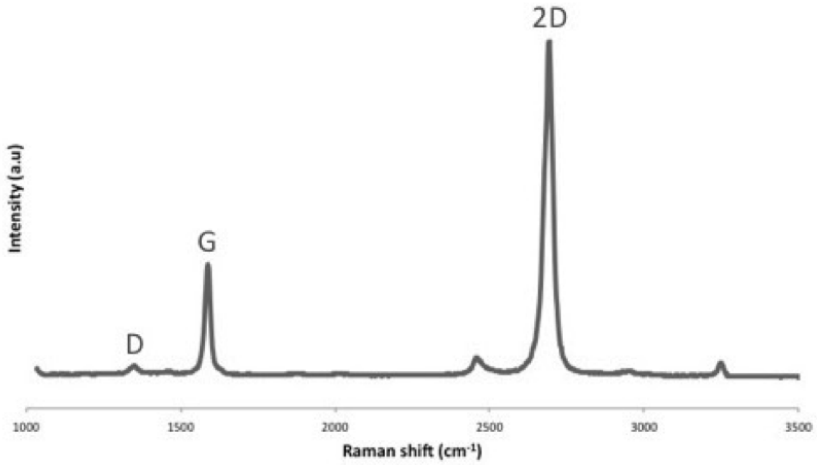

Figure 4.4: Raman spectroscopy of the graphene sample: the D peak is almost absent, revealing that the quality of the material is extremely good.

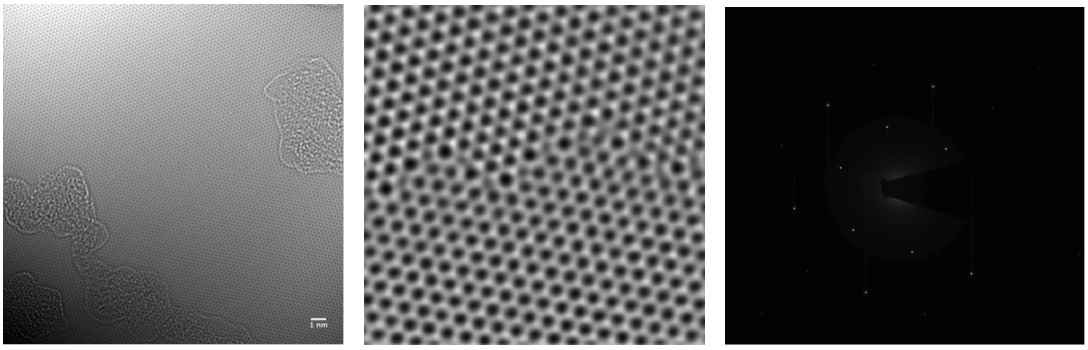

Figure 4.5: HRTEM image of a monolayer of graphene with its hexagonal pattern (left); inset showing a graphene grain boundary: see how the orientation of the material changes (center); SAED of the sample: diffraction condition corresponding to the hexagonal structure are satisfied (right).

Thus, the quality of the graphene film can be extracted from the following peak ratios: 2D/G and D/G. The ratio between the intensity of the 2D peak and the G peak (I_{2D}/I_G) should be greater than 2 while the ratio between the D peak and the G peak (I_D/I_G) should be less than 0.05. These are necessary conditions to define a good quality monolayer graphene. The different Raman parameters result in good values: $I_D/I_G < 0.05$ and $I_G/I_{2D} = 0.4 - 0.7$ depending on the scanned area, while the peak width is given by the Full Width at Half Maximum (FWHM) which for the G peak is $16 - 22cm^{-1}$ and for the 2D peak is $33 - 37cm^{-1}$. TEM analysis also confirms that the quality of graphene is high (Figure 4.5). A more detailed inset of a graphene grain boundary shows a where the hexagonal structure of carbon atoms slightly changes its orientation.

4.9 Characterization of CVD commercial h-BN: Monolayer and Multilayer

In this section, we will characterize Monolayer and Multilayer h-BN from Graphene Supermarket [42], that is, up to now, the only commercially available CVD h-BN. Both materials were received grown on Cu foils. Before performing the transfer, CVD h-BN must be characterized on Cu to check the quality, paying attention to the most general features of the film. Especially, multilayer h-BN growth with uniform thickness is also one of the most important requirements in 2D h-BN, because monolayer h-BN is not thick enough to inhibit the electron transport through the h-BN layer in the surface normal direction and any influence of substrate morphology or roughness underneath the h-BN [33]. Optical images at low magnification of h-BN Monolayer on Cu and h-BN Multilayer on Cu are shown in Figure 4.6. h-BN Monolayer sample shows a variation of larger (up to $1mm$) and smaller (hundreds of μm) copper grains; those darker spots, pointed out by red arrows, could indicate that the copper was very close to the melting temperature due to the process recipe. This could have compromised the quality of the grown material. On the other hand, h-BN Multilayer on copper looks slightly different. Copper grains are smaller in size (tens of μm), probably due to a shorter annealing time of the copper. Nevertheless, even for h-BN Multilayer we have dark spots where the Cu was close to the melting point and the quality of the material might not be optimal.

A deeper characterization is only possible transferring onto a specific substrate.

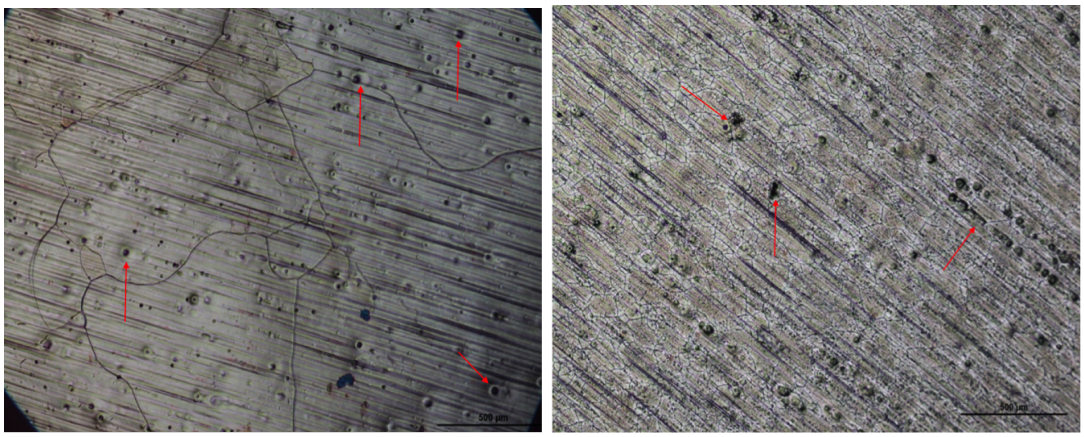

Figure 4.6: Low magnification images of h-BN Monolayer (left) and h-BN Multilayer (right) on copper. Red arrows points out spots where probably the copper has melted.

For this reason, we transferred a 1x1cm^2 of both h-BN Multilayer and h-BN Monolayer onto a 1x1cm^2 300nm SiO_2/Si substrate by using the wet transfer process (Section 4.1). As expected, the h-BN Monolayer (Figures 4.7a and 4.7b) samples show a low contrast with respect to the substrate while in the h-BN Multilayer (Figures 4.7c and 4.7d) the contrast is well defined. At higher magnification, blue arrows point out some shiny spot lines as well as circular features, which are probably due to a contamination coming from the growth process. However, we could observe the presence of these features in one of the batches and this leads us to another important aspect: the lack of reproducibility between batches. Figure 4.8 shows that, not only we have a different topography of the material from one batch to another, but differences in homogeneity are apparent even in the same batch. This is an issue that must be taken into account when fabricating heterostructures because it could bring to unwanted and unexpected different performance results.

Then, we proceeded with the characterization both h-BN Monolayer and h-BN Multilayer with Raman spectroscopy. Gorbachev et al. [32], have proved how Raman spectroscopy is an effective, nondestructive, technique to identify exfoliated h-BN Monolayer flakes. Unlike in graphene, h-BN measurements were carried out with 5s of integration time and 15 accumulations. According to the literature, the h-BN Monolayer peak for h-BN Monolayer flakes has been found to be around 1368cm^{-1}. On the other hand, the more intense peak of the h-BN Multilayer has been found to be around 1371cm^{-1} due to the expected red shift for the case of a multilayer material [32]. This last peak is also wider. Figures 4.9b and 4.9d shows the Raman spectra of both samples once they have been transferred onto

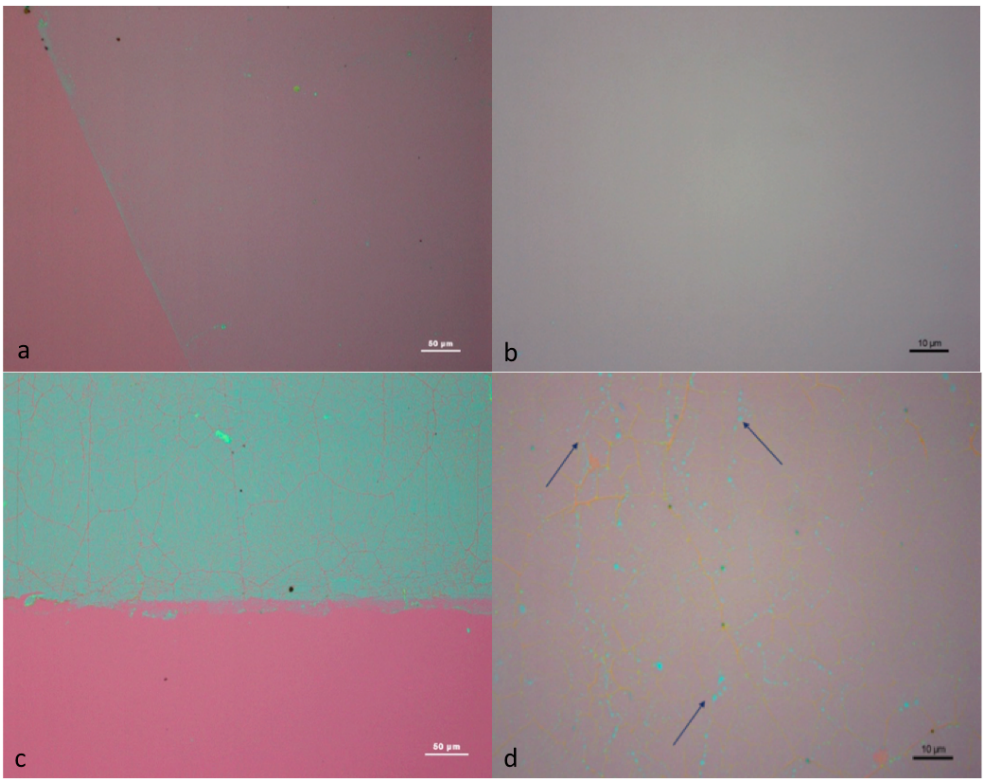

Figure 4.7: a), b) low and high magnification images of CVD h-BN Monolayer; c), d) low and high magnification images of CVD h-BN Multilayer with arrows pointing the contamination coming from the growth. In both samples the substrate is $300nm$ SiO_2.

$300nm$ SiO_2/Si substrate. However, we noticed something interesting performing acquisitions for the h-BN Monolayer sample as shown in Figure 4.9c: we revealed the unexpected presence of two broader peaks centered at $1361cm^{-1}$ and $1595cm^{-1}$ that completely hide the presence of the h-BN peak. Since, to the best of our knowledge, no results have been reported about this type of spectra, we arrived at the conclusion that they might be due to a secondary product coming from the precursor decomposition in the CVD synthesis of the h-BN and that they constitute part of the contamination that affects the quality of the growth. Specifically, in the part of this thesis that focuses on the synthesis of h-BN, we will see how these peaks will appear again in the Raman characterization.

The h-BN Multilayer and Monolayer IR spectra are acquired with 250 scans and $4cm^{-1}$ resolution. SiO_2 background is also acquired with the same settings in order to a have a correct subtraction. Results are more representative than Raman spectroscopy revealing the high effectiveness of this technique and they agree with

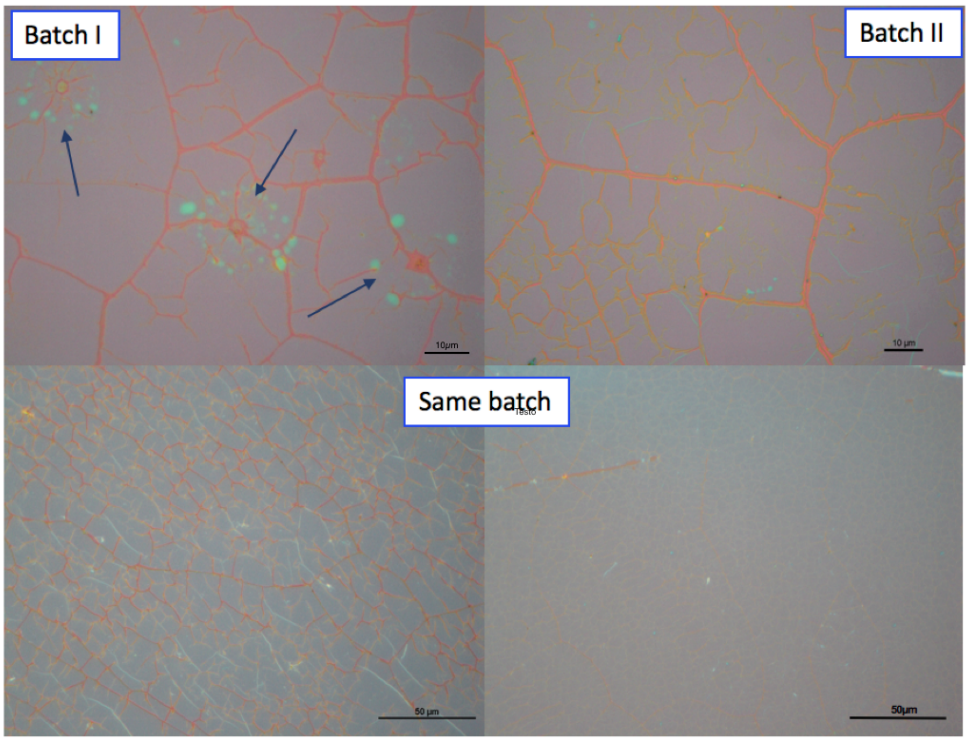

Figure 4.8: Lack of reproducibility of CVD h-BN. As we see, we have differences between the same batch and different batches as well.

the literature [34] which, however, is quite scarce. In Figure 4.9f, besides the CO_2 occurring at frequency greater than $2000cm^{-1}$ and the weak phonon at $\approx 1000cm^{-1}$ coming from the difference in the substrate underneath, we can clearly observe the phonon corresponding to $1365cm^{-1}$, which confirms the presence of the BN with a hexagonal planar structure. Clearly, the most intense phonon corresponds to the h-BN Multilayer sample. On the other hand, the expected phonon at $805cm^{-1}$ is often weak unless you do ATR (Attenuated Total Reflection) measurements and in this case, we could not reveal it.

Transmission Electron Microscopy was performed only for h-BN Monolayer sample. Selected Area Electron Diffraction (SAED) (Figure 4.10b) confirms the hexagonal structure of the material and in the high-resolution image (Figure 4.10a) we can directly see the hexagonal pattern formed by boron and nitrogen atoms covered by some organic contamination. Figure 4.10a also shows something interesting: among the film some triangle-shaped defects can be identified thanks to a different contrast with respect to the hexagonal pattern. The reason of this shape is because all the

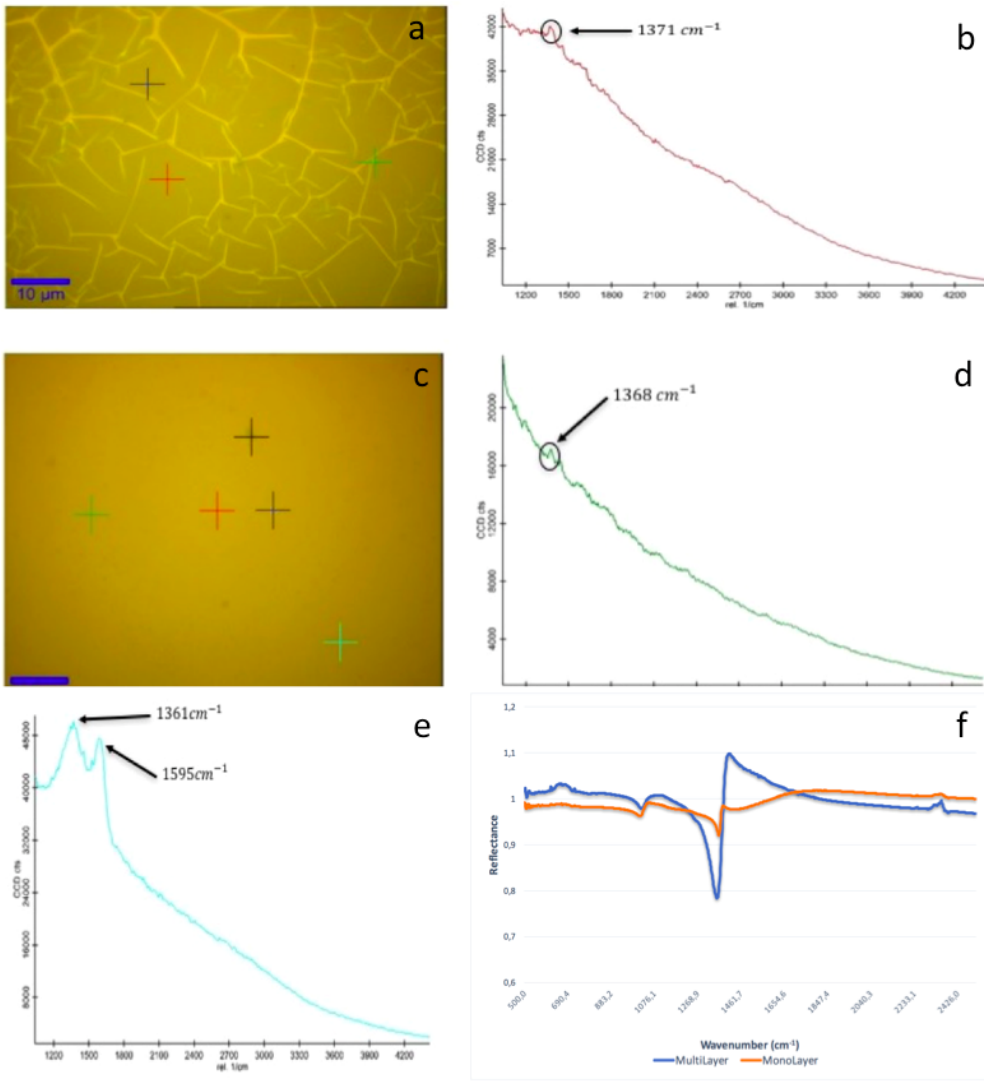

Figure 4.9: a) Optical image at Raman microscope of CVD h-BN Multilayer; b) Raman spectroscopy of CVD h-BN Multilayer with the characteristic peak at 1371cm^{-1}; c) Optical image at Raman microscope of CVD h-BN Monolayer; d) Raman spectroscopy of CVD h-BN Monolayer with the peak at 1368 cm^{-1}; e) Raman signal of the contamination with two broader peaks centered at 1361cm^{-1} and 1595cm^{-1}. The h-BN peak is fully hidden; f) IR spectroscopy on CVD h-BN Monolayer (orange) and CVD h-BN Multilayer (blue).

atoms forming the edge termination are of the same type thanks to the difference in mass between B and N (see also Section 3.2).

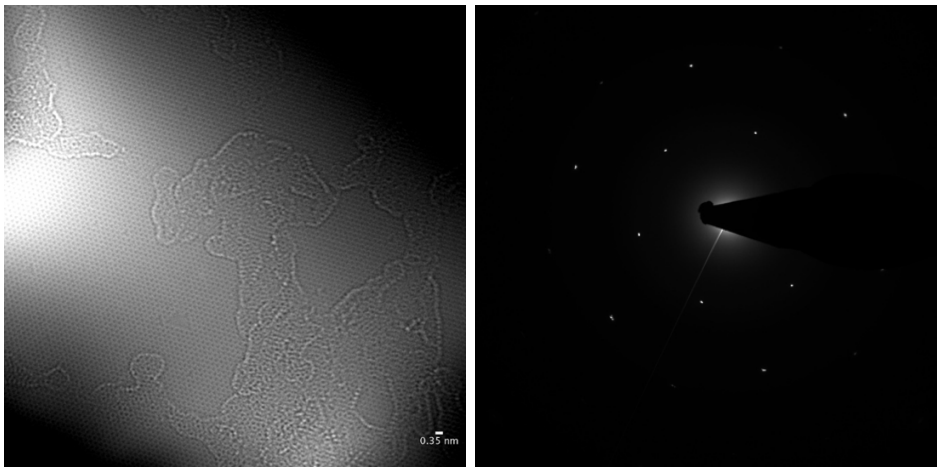

Figure 4.10: a) HRTEM image of CVD h-BN Monolayer showing the hexagonal pattern of the material. Triangles with different constrast are defects. b) SAED of a CVD h-BN Monolayer sample confirming the hexagonal structure;

The h-BN samples analyzed above are, nowadays, the unique example of commercial hexagonal boron nitride grown by chemical vapor deposition method. Although the overall quality of the film can be improved and the reproducibility is not guaranteed, they represent a real opportunity to grow a good quality h-BN through chemical vapor deposition with even the possibility to control the number of layers. Hence, the actual need of growing large scale CVD graphene, urge the research to put besides this material a wide available large scale CVD h-BN that would represent an important step towards the development and the future implementation of electronics based on 2D materials into our daily life. For this reason, in the next chapter we will focus on the synthesis of hexagonal boron nitride via chemical vapor deposition, describing the setup of the equipment carried out in this thesis, the growth conditions and the characterization of the output material of the most relevant runs.

Chapter 5

CVD h-BN synthesis

5.1 Furnace setup

In this thesis work we performed hexagonal boron nitride growth using high vacuum chemical vapor deposition (HVCVD) on polycrystalline Cu foils and ammonia borane as precursor. Choosing the best set up for the growth was not an easy operation. In Figure 5.1 the final set up of the HVCVD is represented. The ammonia-borane precursor is placed in a custom-made bubbler and connected to a $55mm$ diameter quartz tube placed in a tubular furnace (Carbolite Gero, 3216/P1P5) and the sample is placed at the center of the tube lying on the bottom of a ceramic boat. The bubbler is wrapped by heating tapes and "ON/OFF" temperature controller is used to set the suitable temperature conditions for decomposing of the precursor. Unfortunately, this type of controller does not represent the optimal solution, since the set temperature is always reached with an undesired overshooting up to 10%: the best solution in this case, could be use a different type of controller, for example a PID controller. In order to create high vacuum, high vacuum clamps and high vacuum metal rings are necessary in each joint and all the system is connected to a high vacuum pump (PFEIFFER, HiCube 80 ECO) which could ideally achieve a pressure of $10^{-5}mbar$. A mixture of hydrogen and argon (15% H_2, 85% Ar) is used as carrier gas to supply the evaporated ammonia-borane into the furnace and its flow is controlled both from a leak pressure valve (VAT, Series 590 DN 16mm) and a flow mass meter (RS, MR 3000). The initial desired pressure of $10^{-5}mbar$ is measured with a high vacuum sensor (PFEIFFER, PCR 280).

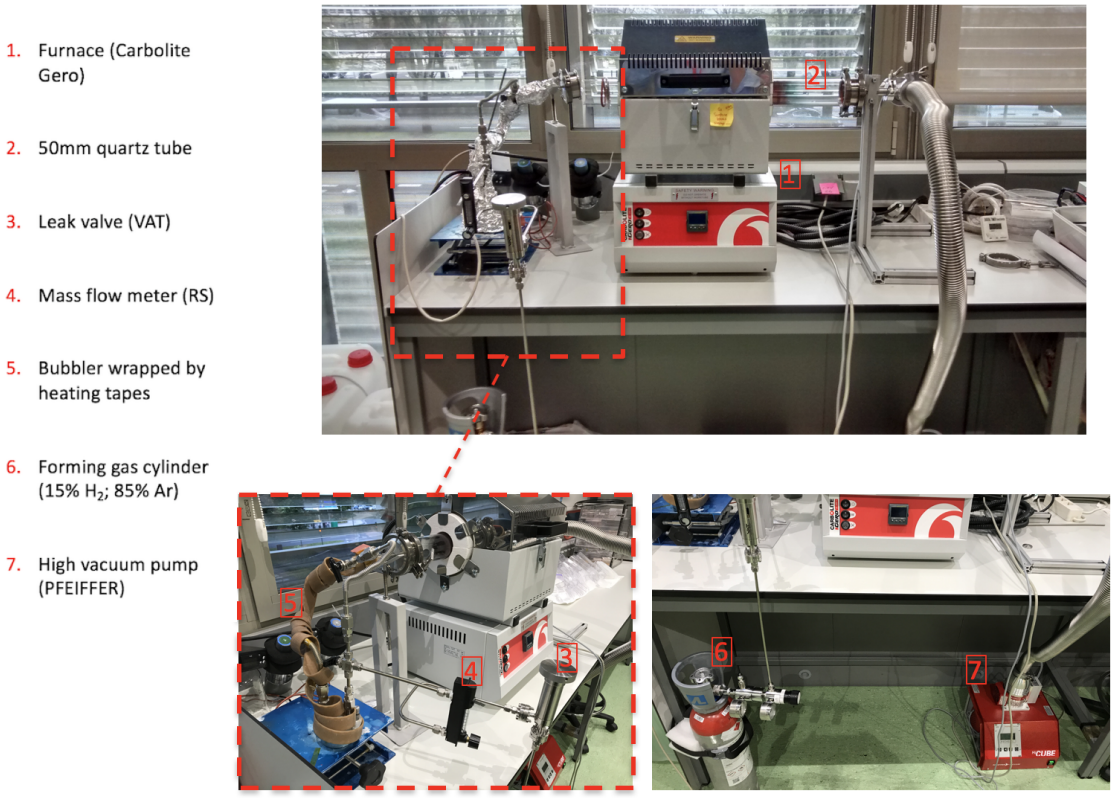

Figure 5.1: Set up of the HVCVD is represented

5.2 Characterization of grown h-BN

Starting the synthesis of a 2D material is not immediate and requires many attempts in order to get a good quality output. We will call each run with the label "G # of the growth". As for the graphene synthesis, the growth consists in two steps: Cu annealing and layer synthesis. Table 5.1 presents a summary of the growth conditions of the most relevant and successful growths (G1, G2, G5, G9, G10).

As for the Graphene Supermarket h-BN we characterized our CVD h-BN with different methods. In order to perform all the needed measurements, we first transferred each 1x1cm^2 sample from Cu to a 300nm SiO_2 substrate using a standard wet transfer method.

	G1	**G2**	**G5**	**G9**	**G10**
Growth Temperature	$1000°C$	$1000°C$	$980°C$	$960°C$	$960°C$
Growth Time	20 min	30 min	10 min	25 min	10 min
Ammonia Temperature	$\approx 120°C$	$\approx 120°C$	$\approx 90°C$	$\approx 90°C$	$\approx 90°C$
Ammonia Time	$\approx 0.4g$	$\approx 0.08g$	$\approx 0.08g$	$\approx 0.05g$	$\approx 0.05g$
Annealing Time	10 min	10 min	10 min	60 min	60 min
Leak Valve Turn	Annealing: 7.5 Growth: 3.5	Annealing: 7.5 Growth: 3.5	Annealing: 7.5 Growth: 1.0	Annealing: 7.5 Growth: 0.25	Annealing: 600 sccm Growth: 200 sccm
Pressure (mbar)	Annealing: $8.6 \cdot 10^{-3}$ Growth: $1.4 \cdot 10^{-2}$	Annealing: $7.4 \cdot 10^{-3}$ Growth: $8.6 \cdot 10^{-3}$	Annealing: $7.4 \cdot 10^{-3}$ Growth: $8.6 \cdot 10^{-3}$	Annealing: $7.7 \cdot 10^{-3}$ Growth: $9.2 \cdot 10^{-3}$	Annealing: $7.7 \cdot 10^{-3}$ Growth: $2.4 \cdot 10^{-3}$

Table 5.1: Summary of the most relevant runs for the h-BN CVD synthesis.

In G1 the ammonia borane (Sigma Aldrich, 99.7% pure) quantity was enough to cover the base of the bubbler while the growth temperature was set in order to get the substrate as close as possible to its melting point. All the other parameters were set similar to previous reports (see section CVD Hexagonal Boron Nitride). High magnification optical images and Raman mapping (Figures 5.2a and 5.2b), show that G1 is full of wrinkles and contaminated by a non-homogeneous pattern extending all over the sample. This leads to a very high contrast with the substrate, which is not in agreement with what we said in previous sections. However, we decided to perform Raman and IR spectroscopy which, in any case, confirmed the absence of h-BN on the sample (Figures 5.2c and 5.2d).

We attributed the contamination of the sample to the (relative) high quantity

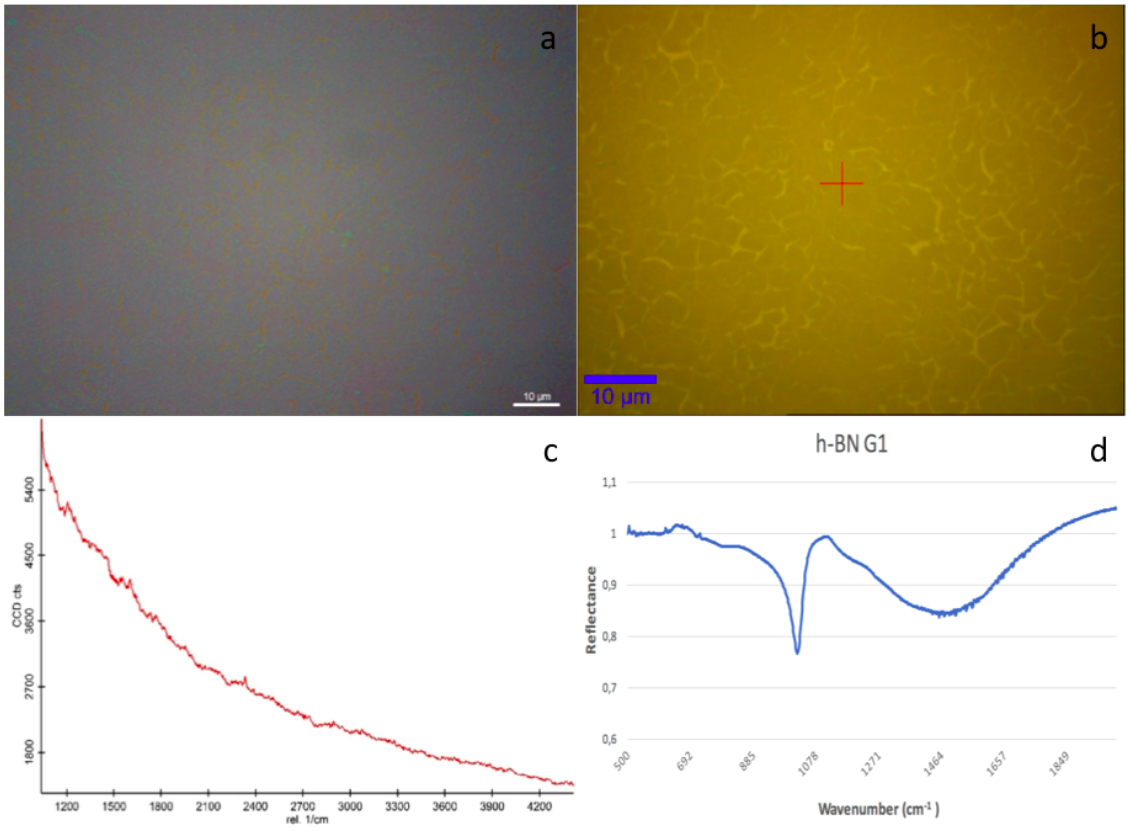

Figure 5.2: G1 characterization: a) high magnification optical image of the sample transferred onto $300nm$ SiO_2; b) Optical image at Raman microscope of the sample; c) Raman signal corresponding to the red cross on the Raman map; d) IR signal of the sample.

of ammonia borane inside the bubbler. Thus, for G2 we decreased the amount to $0.08g$, weighed with a high precision balance. Unfortunately, even this time high magnification optical images show that G2 looks fully contaminated by those that seem grainy BN particles (Figures 5.3a and 5.3b). We might think that this contamination is coming from a secondary reaction product of the precursor evaporation and that the forming gas, flowing through the bubbler, was responsible for blowing some precursor particles inside the tube. Raman spectroscopy (Figure 5.3c) of G2 was similar to that acquired on some particle impurities on the Graphene Supermarket h-BN (see Section 4.9), with 2 relevant peaks at around $1360cm^{-1}$ and $1595cm^{-1}$ and 2 less strong peaks centered at $2691cm^{-1}$ and $2929cm^{-1}$. Thus, the idea was that the BN particle contamination was so strong that h-BN was hidden below all

this contamination. IR spectroscopy on G2 partially confirmed our hypothesis (Figure 5.3d): the weak phonon at $\approx 1365cm^{-1}$ reveals the presence of some h-BN on the sample.

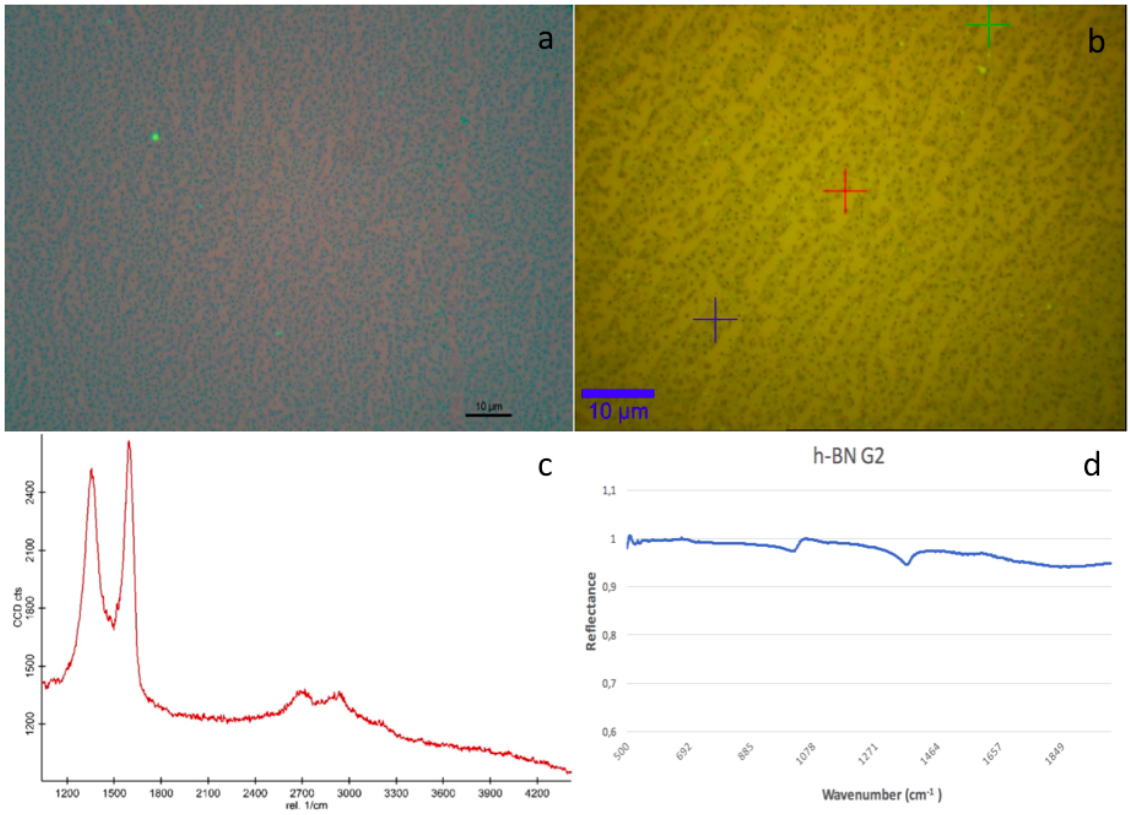

Figure 5.3: G2 characterization: a) high magnification optical image of the sample transferred onto $300nm$ SiO2; b) Optical image at Raman microscope of the sample; c) Raman signal corresponding to the red cross on the optical image at Raman microscope: the pronounced peaks at around at $1360cm^{-1}$ and $1595cm^{-1}$ fully hide any presence of h-BN; d) IR signal of the sample showing a small peak of h-BN.

Therefore, we decided to perform TEM analysis of G2. Selected Area Electron Diffraction (SAED) was also used in order to check the crystallinity of the material (Figure 5.4a). As one can see, hexagonal diffraction points are not well defined meaning that other diffraction conditions are satisfied: this suggests that crystallinity of the sample is not homogeneous and amorphous contamination is extended all over the sample. On the other hand, HRTEM images (Figure 5.4b) gave very interesting results: a h-BN monolayer grain is visible as well as bilayer and tri-layer regions where a hexagon structure is more defined. From the first trials, we mainly had

two problems: contamination, in different forms, extended all over the sample, and copper evaporation. In particular, copper evaporation not only contaminates all the quartz tube but is even responsible of sticking the samples to the bottom of the ceramic boat.

XPS analysis also confirms the presence of the h-BN: B 1s and N 1s components are consistent with those of h-BN (190.6eV and 398eV respectively) with a ratio close to 1:1. In both materials we also have a peak at higher binding energy, probably due to some oxidized species (e.g. B_2O_3) (Figures 5.4c and 5.4d).

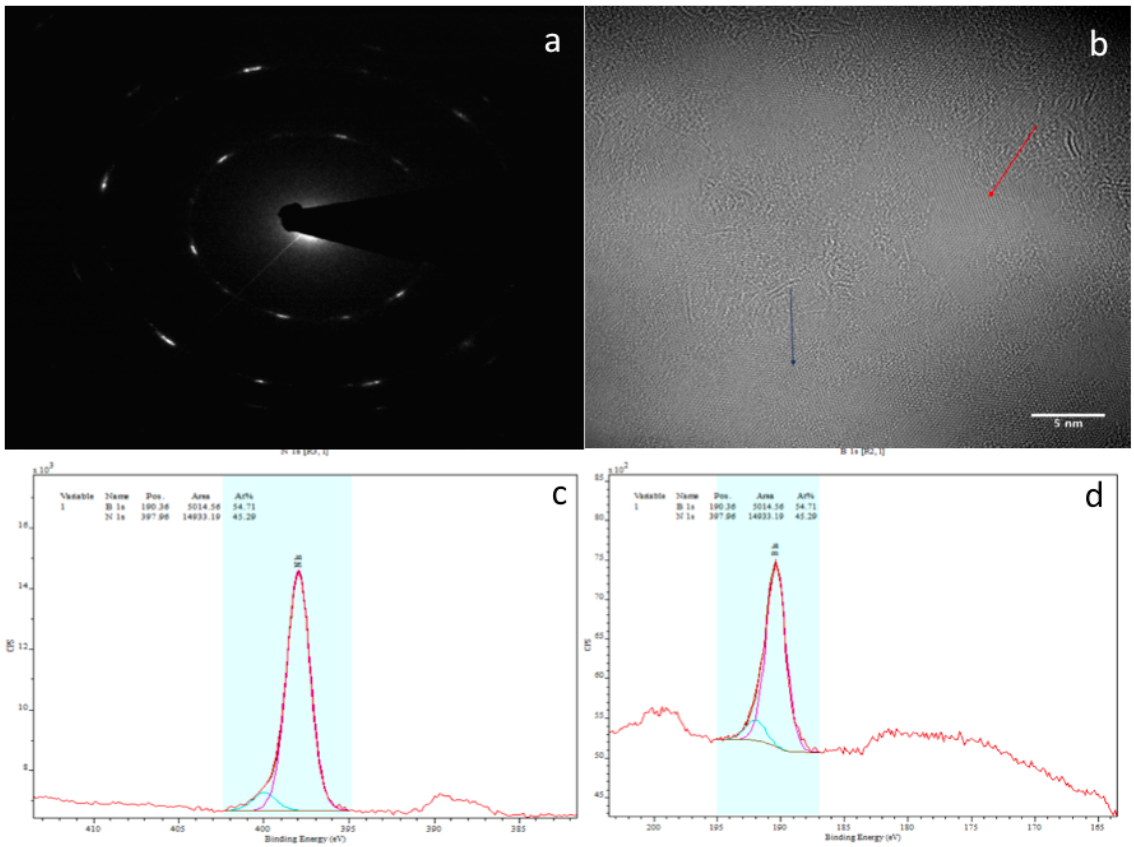

Figure 5.4: G2 characterization: a) HRTEM image of the sample: red arrow and blue arrow show a monolayer and multilayer regions respectively; b) SAED of the material; c) d) XPS sample analysis showing a B:N ration close to 1:1. Both elements are fitted with at least 2 components.

Then in G5 growth temperature was decreased from the initial value of 1000°C to 980°C. In fact, the melting point of the copper at standard pressure is 1084.6°C but considering the high vacuum conditions, it considerably decreases close to 1000°C. On the other hand, to overcome the problem of the contamination, we drastically

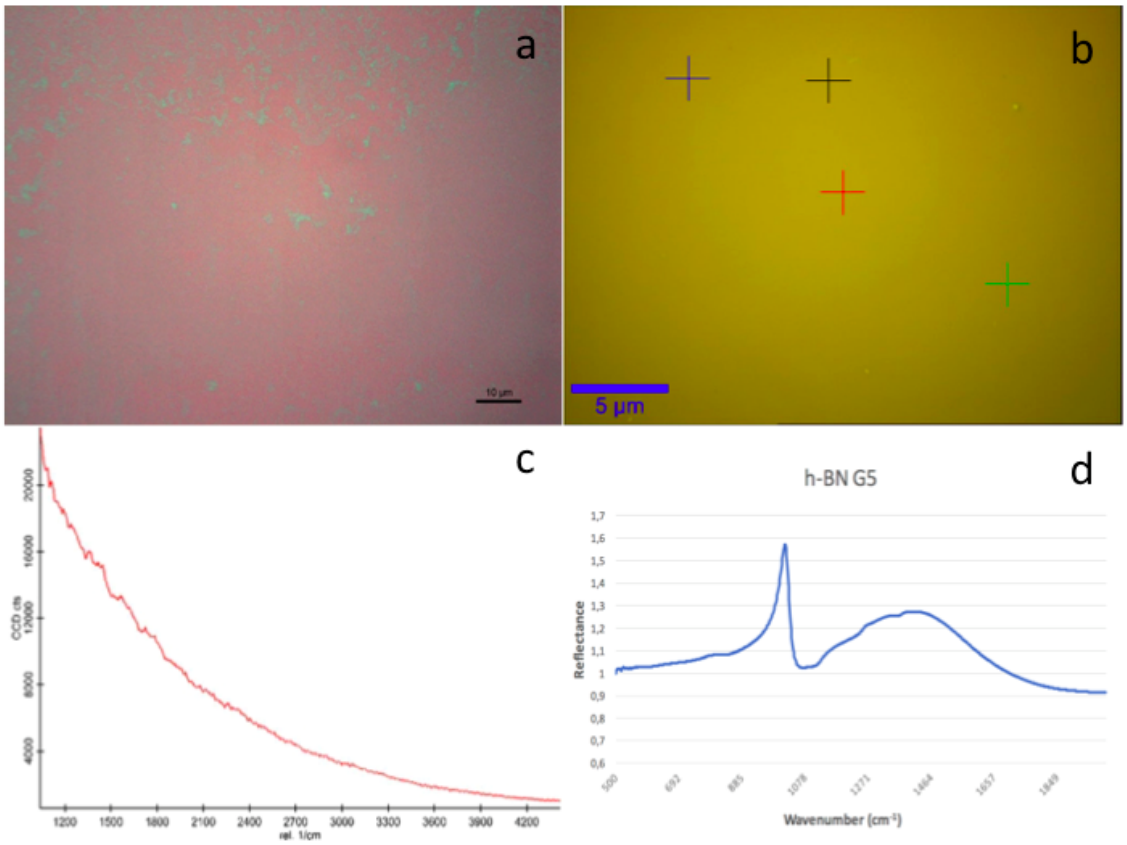

Figure 5.5: G5 characterization: a) high magnification optical image of the sample transferred onto 300nm SiO2; b) Optical image at Raman microscope of the sample of the sample; c) Raman signal corresponding to the red cross on the optical image at Raman microscope of the sample revealing no h-BN d) IR signal of the sample

decreased the precursor feeding rate during the growth limiting the leak-valve turns to 1 and decreasing the precursor temperature down to 90°C in order to limit the precursor reaction as well. As optical characterization shows (Figure 5.5a), some areas have a lower contrast than in previous growths and they seem free of contamination. Then, even if the growth is not homogeneous, this confirms the idea that the precursor feeding rate is a crucial factor in order to get a high-quality material. However, Raman spectroscopy was not able to reveal any significant peak around 1365cm^{-1}. IR neither gave us relevant results since no h-BN phonon was detected (Figures 5.5b, 5.5c and 5.5d).

To reduce of the contamination even more, in G9 and G10 we decreased the quantity of the precursor inside the bubbler down to 0.05g and limited the leak-valve turns to a quarter of a turn. For G10, we give the value of the forming gas

flow in *sccm* since we could measure it with a flowmeter. Then, in G9 and G10 we performed a very long annealing of the substrate (60 min). It is well known that the longer the annealing, the smoother the catalyst surface and larger the formation of copper grains in order to get better h-BN quality. This avoids nucleation sites and gives as large as possible h-BN triangle shaped domains, which are crucial for various applications of h-BN films, especially in high-performance G/h-BN devices [26].

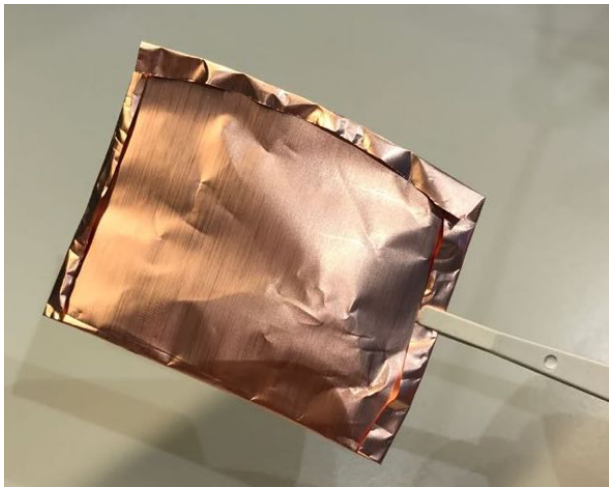

Figure 5.6: Example of an enclosure shape structure for copper. Edges are closed to prevent particles to contaminate the inner part.

Nucleation density can be controlled also with the combination of a reduced feeding rate of the precursor and an enclosure shape structure of the copper substrate, that consists in folding a copper foil on itself (closing then the edges) such that we have an inner surface and an outer surface (Figure 5.6). At the same time, the enclosure shape structure is needed because of the etching effect of the hydrogen flowing through the tube during the growth.

Apparently, the hydrogen etching reaction on the outer surface exposed to Ar/H_2 carrier gas is much faster than that of the inner surface. As a result, relatively high precursor feeding rate is necessary for the outer surface in order to surpass the hydrogen etching reaction and grow some h-BN, while in the inner surface, the hydrogen reaction occurs less and the feeding rate can be lower. Thus, we used the enclosure shape structure for G10 and we analyzed just the inner face of the sample.

Optical characterization of both samples confirmed our hypothesis about precursor particles since surfaces are smoother than previous attempts (Figures 5.7a and 5.9b). G10 in particular, shows a very low contrast with respect to the substrate.

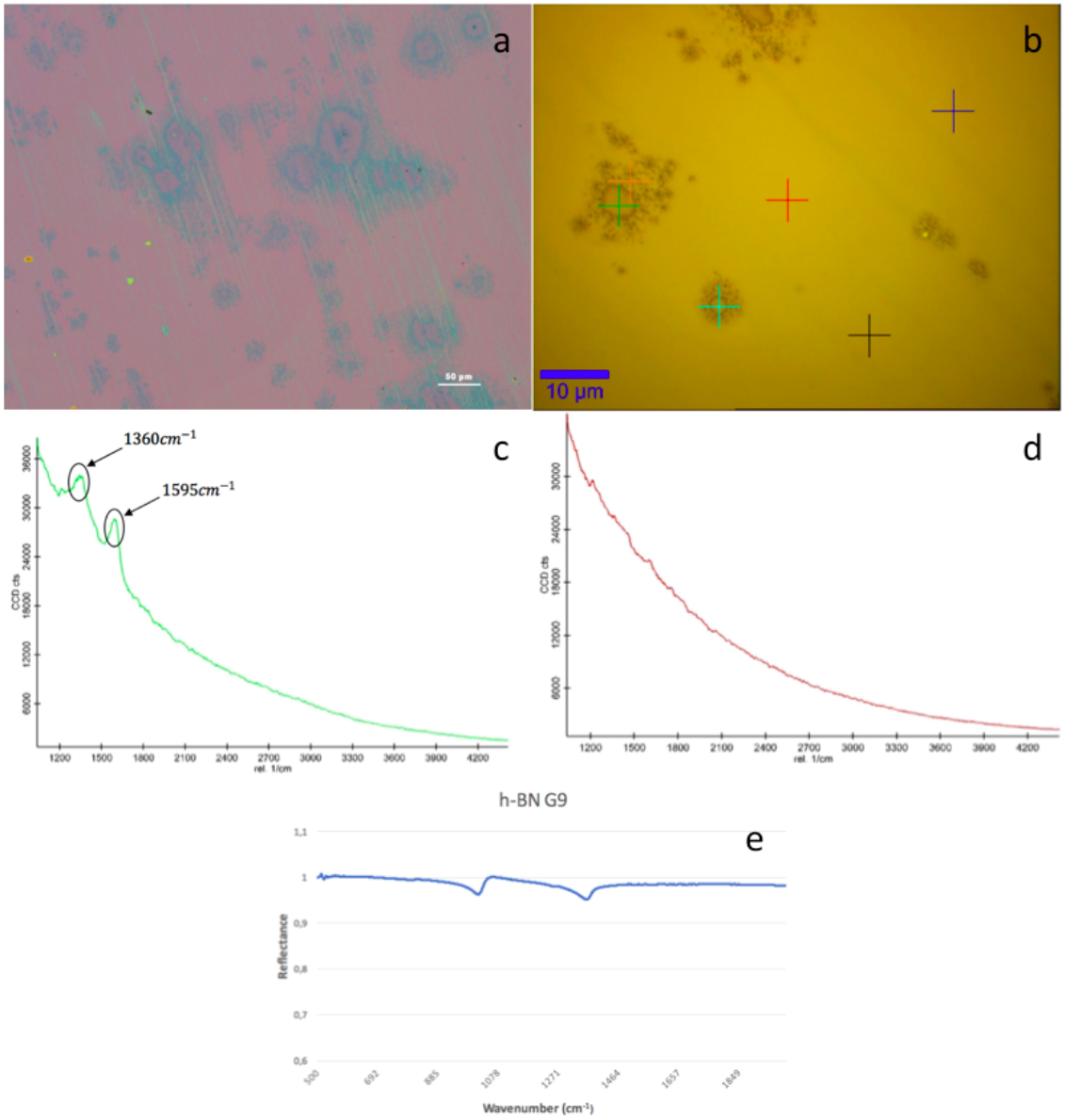

Figure 5.7: G9 characterization: a) high magnification optical image of the sample transferred onto 300nm SiO2. Here the contamination is almost absent; b) Optical image at Raman microscope of the sample of the sample; c) d) Raman signal corresponding to the green and red crosses on the optical image at Raman microscope of the sample: especially on defects, the pronounced peaks at around 1360cm^{-1} and 1595cm^{-1} reveal the presence of some contamination; e) IR signal of the sample showing a small peak of h-BN.

We might think that the enclosure shape structure prevented the inner face from any kind of contamination in the flowing in the chamber. However, not only Raman

spectroscopy does not show any h-BN signal, but in G9 the green spectrum, corresponding to an acquisition on one of the defects, revealed the two peaks centered in $1360cm^{-1}$ and $1595cm^{-1}$, showing that some contamination, even in little amount, is still present (Figures 5.7b, 5.7c, 5.7d and Figures 5.9b, 5.9c). Instead, IR spectroscopy shows different results: in G9 (Figure 5.7e)we have both the presence of the h-BN peak and the one coming from the substrate while in G10 (Figure 5.9d) the h-BN phonon is not defined at all.

Based on the results we got for G2, we decided to perform TEM analysis on G9. Both low resolution images and SAED show that the material looks very disordered (Figures 5.8a and 5.8b). This is probably due to the lower temperature of the furnace during the growth, which, from one side avoids copper evaporation but does not allow the growth of an ordered material. Due to the disordered structure of the material, we could not acquire high resolution images. However, XPS results confirm the presence of the h-BN. Boron is made up of 2 components, the main of which (centered at $190.6eV$) is consistent with that of h-BN: again, there is also a weaker component at higher binding energy probably due to oxidized species. Differently from G2, here nitrogen can be fitted with one component, corresponding to that of h-BN peak in literature ($398eV$). The ratio is 1:0,81 with excess of boron (Figures 5.8c and 5.8d).

5.3 Conclusions about growths

Considering the characterization above, G2 and G9 result in the best growths among all the others. In both cases, we could reveal the presence of some h-BN thanks the to the IR spectroscopy which turns out to be the most effective (and easily accessible) characterization method. From an optical point of view, G9 looks cleaner than G2 meaning that the HVCVD process is extremely sensitive to the flow and the temperature of the precursor. On the contrary, TEM analysis showed how G9 is extremely disordered when compared to G2. This means that growth temperature must be as close as possible to the melting point of the copper and that some evaporation of the substrate seems to be a constrained drawback to obtain a good quality h-BN film. Thus, flow and temperature of the precursor and growth temperature seem to be the most relevant parameters for the synthesis of the h-BN. Next step for improving the quality could be resetting 1000°C as growth temperature and feeding the precursor with a very low flow of forming gas or, as last option, let the precursor

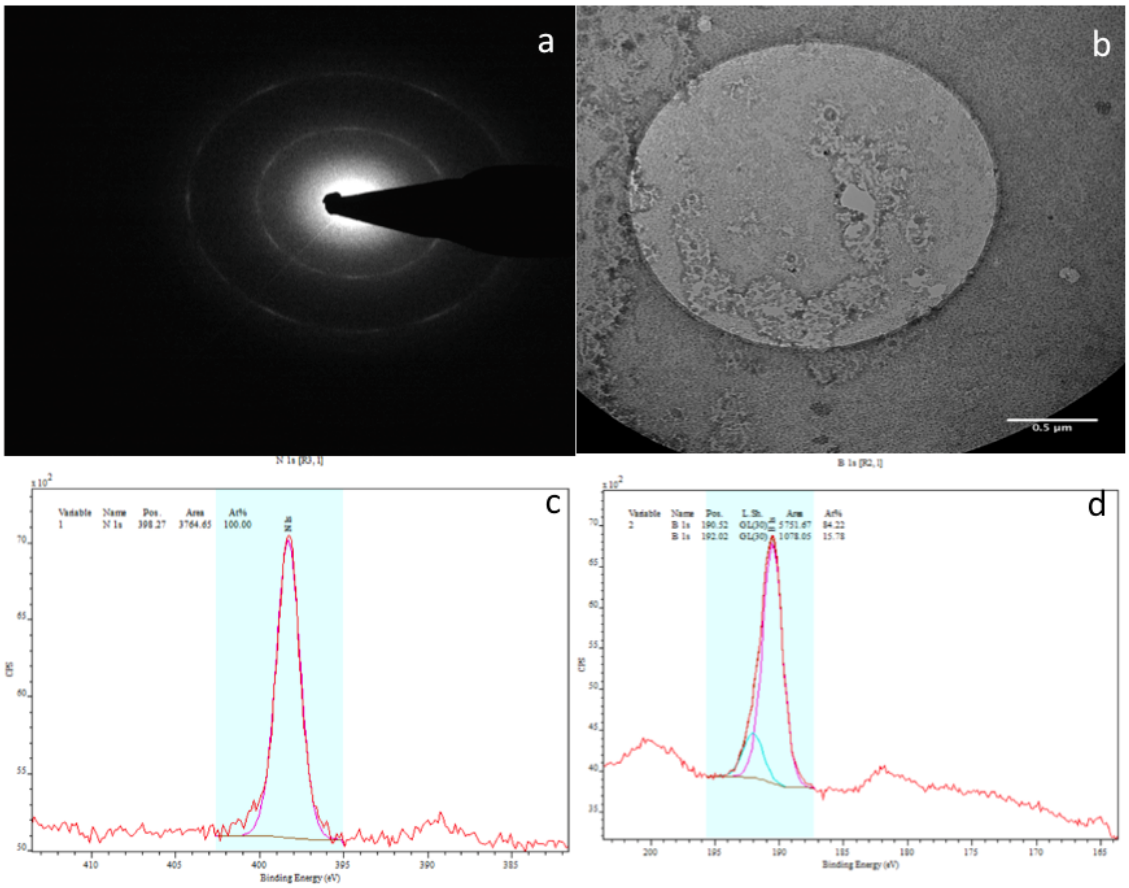

Figure 5.8: G9 characterization: a) SAED of the material showing a that many other diffraction conditions are satisfied besides the hexagonal structure; b) TEM image of the sample: as we see the material is very disordered; c) d) XPS sample analysis showing a B:N ration close to 1:0.81. Here B is fitted with 2 components.

flow by diffusion and leave the forming gas for the annealing process and the cooling phase of the furnace.

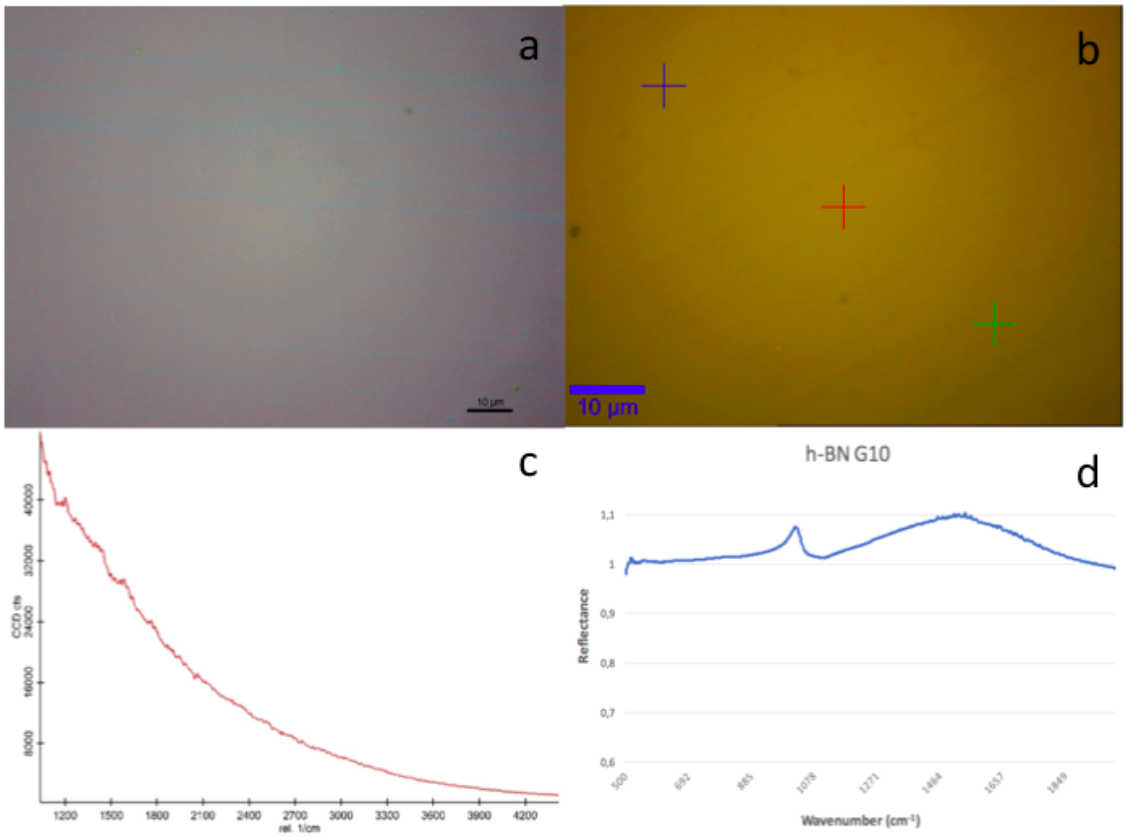

Figure 5.9: G10 characterization: a) high magnification optical image of the sample transferred onto 300nm SiO2. Even for this growth, the contamination is almost absent; b) Optical image at Raman microscope of the sample of the sample; c) Raman signal corresponding to the red cross on the optical image at Raman microscope of the sample with no visible h-BN peak; d) IR signal of the sample.

Chapter 6

Heterostructure fabrication

This last part of the thesis will be fully dedicated to the fabrication and characterization of heterostructures made up with 2D material grown by chemical vapor deposition. The aim is to investigate the effectiveness of the transfer when the CVD h-BN plays the role of encapsulating layer so that we will prepare two kind of stacked samples:

1. CVD h-BN Multilayer/Graphene/300nm SiO_2/Si.
2. CVD h-BN Monolayer/Graphene/300nm SiO_2/Si.

We will first describe the standard method consisting in a standard multitransfer process and the PMMA contamination problems related to it; then, we will propose an alternative solution which allows to create a PMMA free interface between layers in the samples.

6.1 Multitransfer process

A multitransfer process consists in a series of PMMA assisted wet transfer processes (see Section 4.1). Figure 6.1 shows the process for a bilayer heterostructure but the process could be extended to a trilayer sample (sometimes called sandwich structure). Steps a, b, and c show the first standard transfer for the first layer to be transferred: in our case, the bottom layer of the heterostructure is represented by CVD graphene. For this layer, the target substrate will be 300nm SiO_2/Si which will support all the heterostructure. As previously described, several PMMA cleaning methods (solvents, thermal treatments, etc.) could be combined to eliminate the

PMMA protective layer to have a surface as clean as possible on which to deposit the second layer and complete the heterostructure.

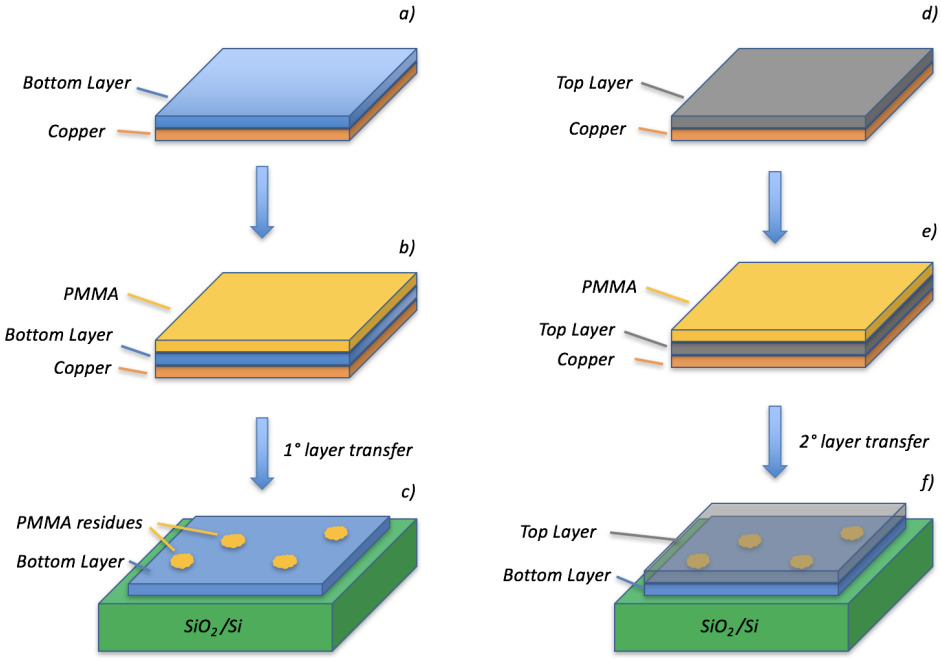

Figure 6.1: Example of multitransfer process: the non-complete removal of the PMMA in step c) contaminates the interface between the top and the bottom layer.

Afterwards, the second transfer for the top layer is performed (steps d and e). This time, the top layer (h-BN) is scooped with the bottom layer/SiO_2/Si structure and the sample is left in an oven at 60°C for a couple of days to get rid of as much water as possible. As one can see, in a multitransfer process we deposit as many number of PMMA layers as the layers involved in the heterostructure. Since standard methods do not assure the complete removal of the PMMA, we would always have some polymer residues contaminating the interface between layers (Figure 6.1f) such that graphene performance could be deteriorated by impurities, scattering centers and doping induced by polymer molecules.

Figure 6.2 shows optical images of both h-BN Monolayer (a and b) and h-BN Multilayer (c and d) heterostructures with such a standard multitransfer process. As we can see, graphene is clearly visible below the h-BN thanks to its multilayer regions proving that the transfer perfectly succeeded. However, both samples are contaminated at the interface from PMMA residues which show up due to the different optical contrast induced by the h-BN.

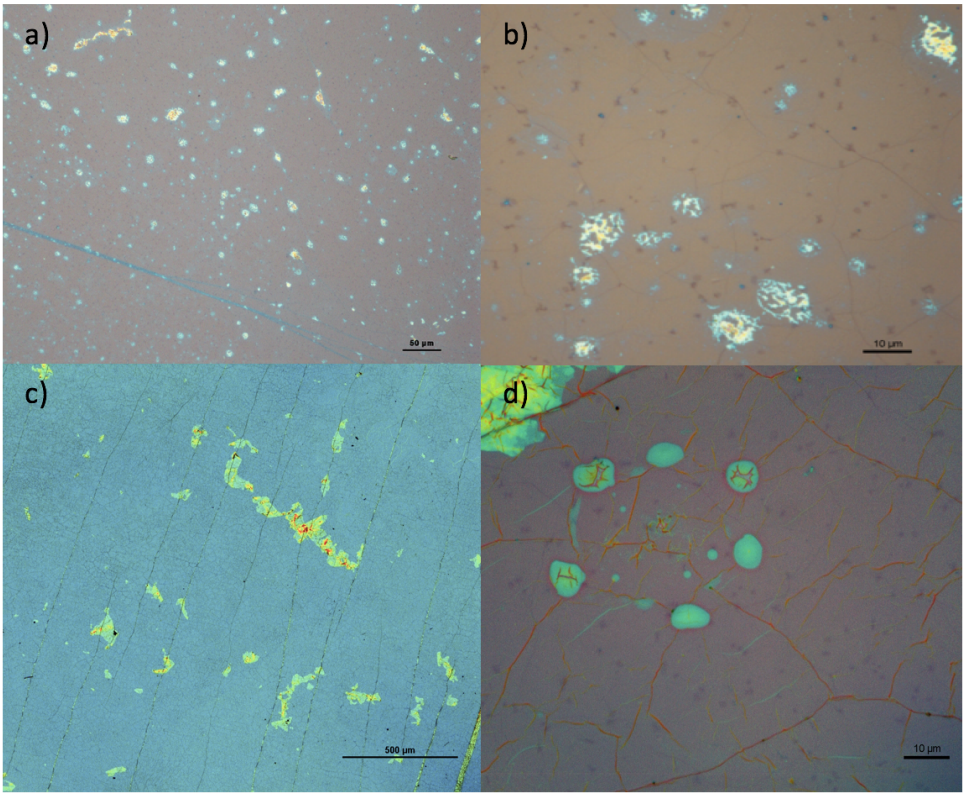

Figure 6.2: a) and b): low and high magnification of CVD h-BN Monolayer encapsulating CVD graphene; c) and d) low and high magnification of CVD h-BN Multilayer encapsulating CVD graphene. In both samples we have a shiny PMMA contamination due to the transfer process.

From here, the necessity to have a transfer method which allows to create a PMMA free interface in the heterostructure in order to get better electrical properties. In the following paragraphs, we will describe this transfer and we will characterize the prepared samples.

6.2 PMMA free interface transfer for CVD materials

Here the top layer is the h-BN Multilayer, while the bottom layer is the graphene. Clearly, inverting the 2D materials, we would have the heterostructure where the CVD h-BN Multilayer plays the role of dielectric layer. We first need to transfer the h-BN film onto the graphene/Cu throughout a standard transfer process described

in Section 4.1 (Figures 6.3a, 6.3b, 6.3c and 6.3d). The only difference here, is that the h-BN Multilayer is scooped with the Graphene/Cu itself. In this way, we will have a clear interface free from any PMMA contamination. Then we apply a thermal treatment for 2h at 150°C in N_2: this step, not only will help to get rid of water residues but will improve the adhesion between the h-BN film and the graphene. The heterostructure is now ready to be transferred onto $300nm$ SiO_2/Si rigid substrate with another standard transfer (Figures 6.3e and 6.3f). Finally, we remove the PMMA layer used to transfer the first layer with solvents.

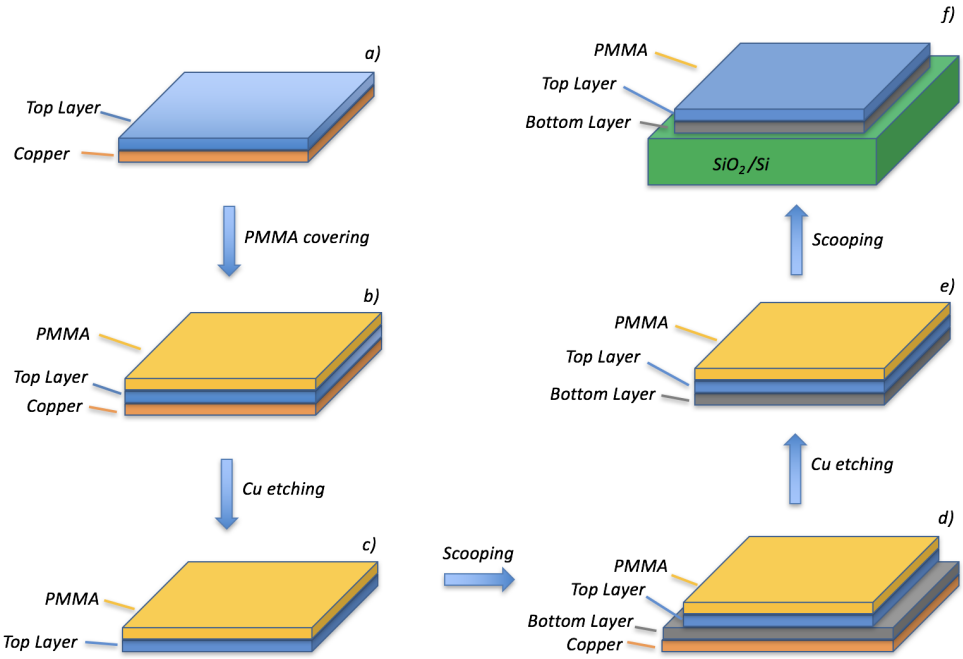

Figure 6.3: PMMA free interface transfer process for CVD materials. In d) the scooping is performed directly with a graphene/Cu substrate avoiding PMMA contamination at the interface.

Results of the transfer are shown in (Figure 6.4). Even in this case, graphene is clearly visible below the h-BN thanks to its multilayer region but this time both samples look much cleaner than in case of a standard multitransfer process. The interface seems free of PMMA contamination and the only residues that seem relevant are those coming from the growth of the h-BN Multilayer (see Section 4.9).

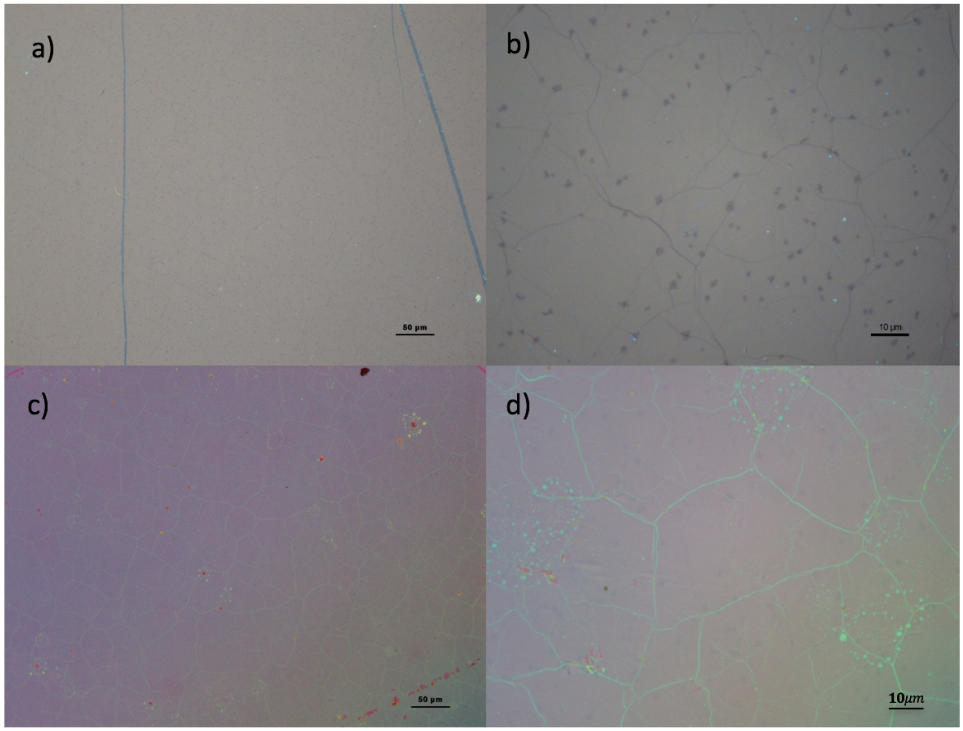

Figure 6.4: Optical results of the PMMA free interface transfer process. a) and b): low and high magnification of CVD h-BN Monolayer encapsulating CVD graphene. c) and d): low and high magnification of CVD h-BN Multilayer encapsulating CVD graphene. Now samples look much cleaner than those in picture (Figure 6.2).

6.3 h-BN flakes exfoliation

The PMMA free interface transfer process is also suitable for heterostructure made up with 2D exfoliated material. In the following, we will show how to adapt the process to an heterostructure in where the h-BN plays the role of encapsulating layer and is prepared using the mechanical exfoliation process. The process of exfoliation is shown in Figure 6.5 [35]. We start by extracting one piece of blue tape [43]. Then, we take transparent PDMS Gel Pack [45] and we cut it into small squares to place them on a microscope glass slide (Figure 6.5b). Then, we select one bulk crystal of h-BN (HQ Graphene [44]) (Figure 6.5a) and we start to exfoliate it using the blue tape; next, the blue tape with the exfoliated material is gently pressed on top of the PDMS stamp (Figure 6.5c) with the aid of a cotton swab and then quickly peeled off from it, resulting in some exfoliated flakes on the stamp. Finally, each stamp is examined in the optical microscope. The contrast of each flake varies with respect

to the thickness. Specifically, we are interested in very low thickness flakes and we should select those that appear most transparent in the optical microscope.

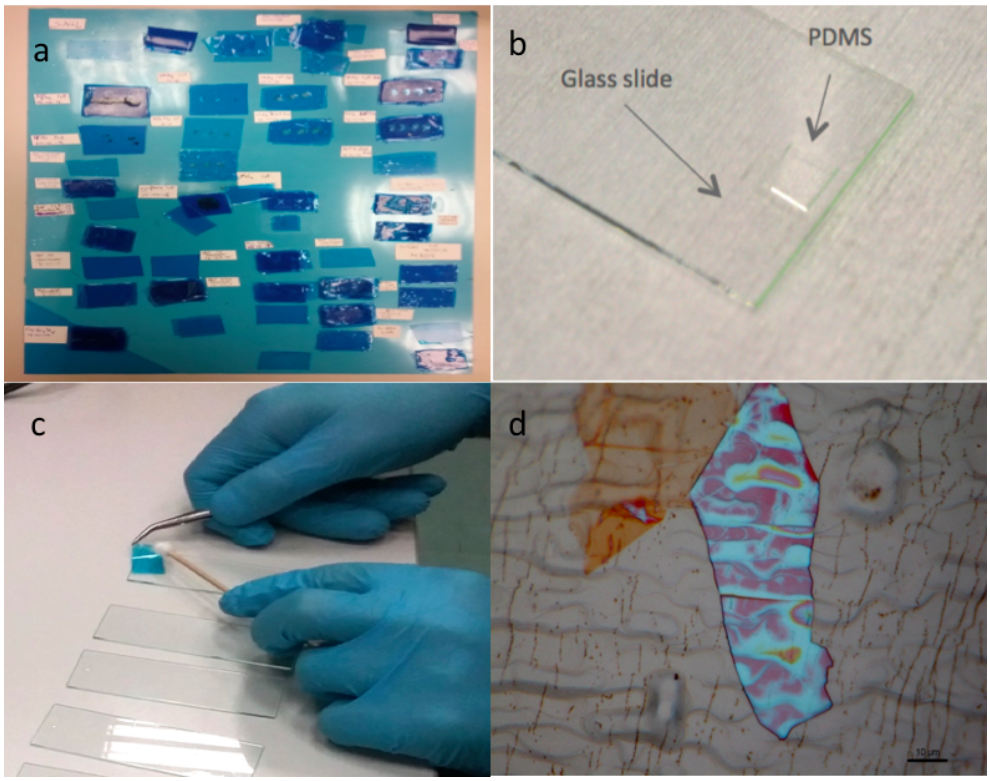

Figure 6.5: a) Table of h-BN bulk crystal protected with blue tape; b) PDMS Gel Pak on top of a microscope glass. c) Pressing and peeling off of the blue tape to exfoliate some flakes; d) h-BN flake deposited on top of graphene/Cu substrate. Here the orange part of the flake is where the flake is thinner.

Once the flake we want to transfer to the substrate has been identified, the glass slide is brought to the stamping system shown in Figure 6.6 and fixed upside-down in a micromanipulator, which allows precise control of the slide in the x axis while the CVD graphene/copper substrate is placed on a translational stage which allows also a rotation movement. The position of the translational stage is fixed, whereas the micromanipulator holding the glass slide has a magnetic base and therefore its position on the board can be easily changed. The rest of the system consists of components to make the transfer visible to us, with a digital camera (Canon EOS 6000-Reflex [46]) as the main component, coupled to a 12X Zoom lens to obtain a higher image magnification. The camera is connected to a TV screen, where the transfer process can be comfortably seen.

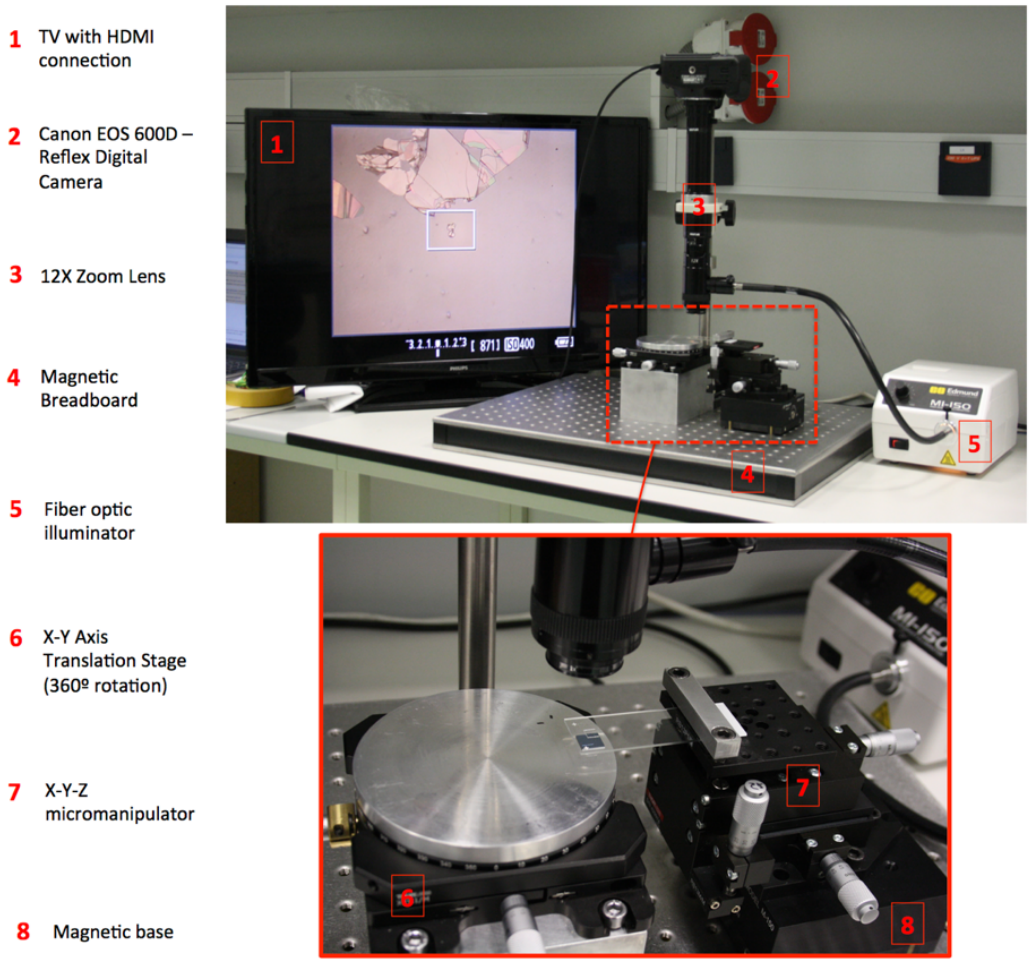

Figure 6.6: Stamping system.

Now, we approach the glass slide to the stage acting on the micromanipulator and on the focus and the magnification of the camera connected to a TV screen. This first part of the transfer relies on the viscoelasticity of the PDMS polymer used: it behaves as an elastic material at short timescales, whereas its viscous property dominates at longer timescales [36]. Practically, if the force that the PDMS stamp applies on the substrate is too large, the results are wrinkles on the flake or air bubbles between the flake and the substrate while when we lift the glass slide, the detachment should proceed as slow as possible. However, we have two main issues that make the stamping operation not so straightforward. One is the low contrast between thin h-BN flakes and copper that reduces the possibility to overhaul if the

flake has been deposited; secondly, we have the high copper roughness ($80 - 100nm$ rms) that leads to a very weak adhesion between the flake and the substrate. These problems make the process with the copper trickier than with a standard SiO_2/Si substrate (roughness $\approx 0.1nm$ rms). Finally, once we verify that (at least) one flake has been deposited (Figure 6.5d), we transfer the h-BN flake/graphene on a rigid substrate.

6.4 Assisted transfer CVD Graphene/ exfoliated h-BN

With reference to the Figure 6.7, we can proceed as a standard assisted PMMA wet transfer process (Section 4.1) and transfer everything on a $300nm$ SiO_2/Si rigid substrate for characterization. The h-BN flake/graphene/Cu sample is first spincoated with some A2 PMMA layer: the only difference here is that the PMMA coating is applied with a slower rotation in order to avoid friction between h-BN flake and CVD graphene which could, someway, compromise the quality of the interface. For the same reason, no magnetic stirring has been used during the whole process (described in Section 4.1). Optical characterization shows that many flakes have been successfully deposited (Figure 6.8) and considering the contrast with the graphene below, we can assume that each flake has a different thickness. The size of the flake is also different from flake to flake: it varies from $\approx 10\mu m^2$ (Figure 6.8c) up to $\approx 40\mu m^2$ (Figure 6.8a).

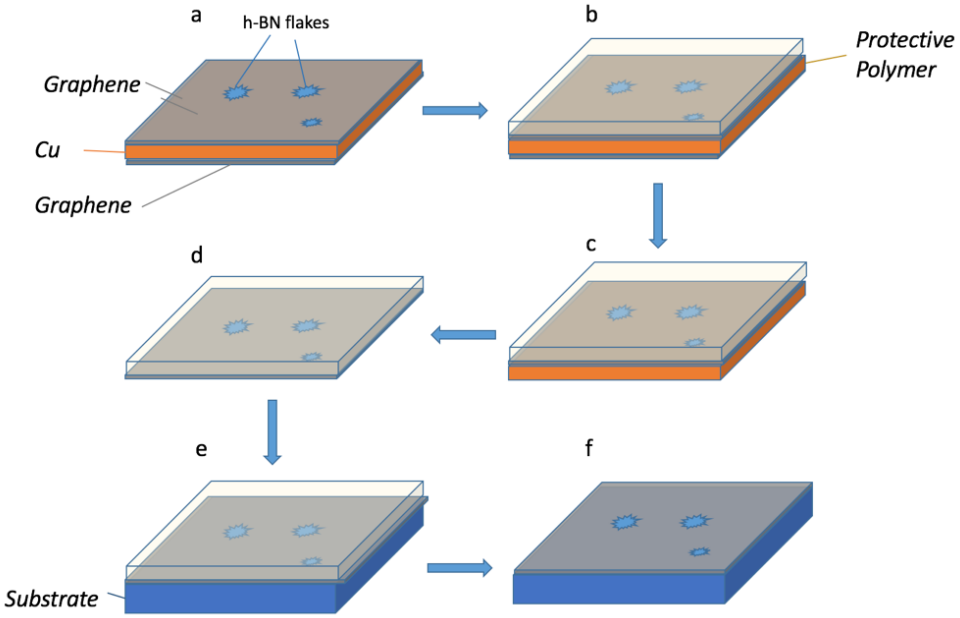

Figure 6.7: PMMA free interface transfer process in case of exfoliated h-BN/CVD graphene heterostructure.

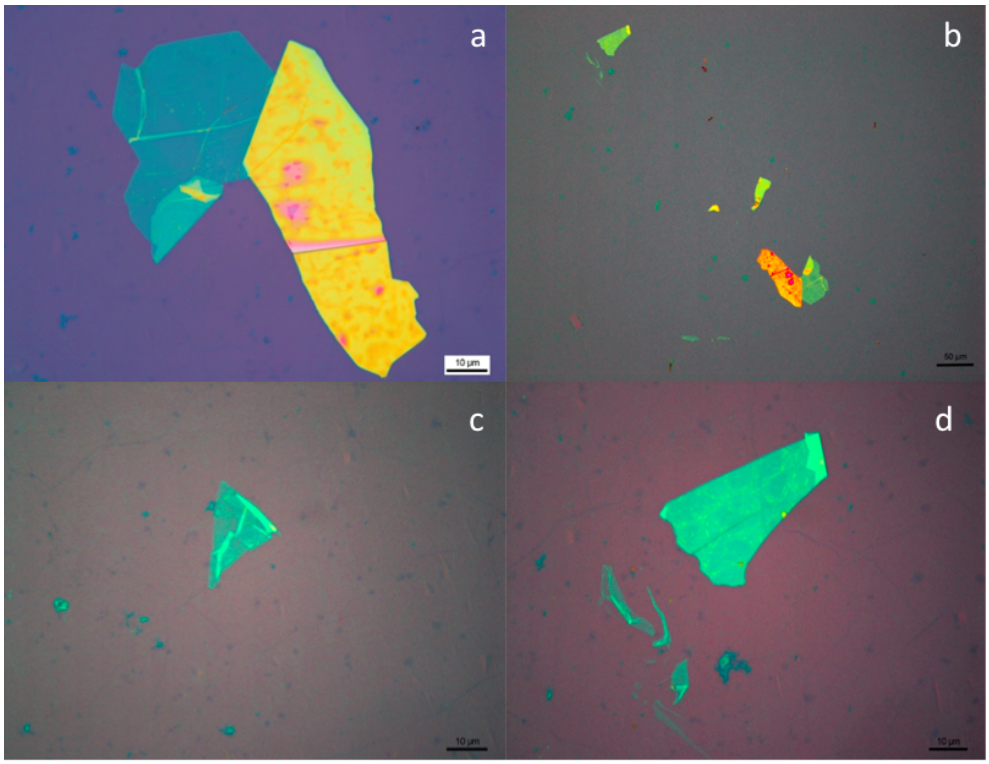

Figure 6.8: Optical results for the PMMA free interface transfer process in case of exfoliated h-BN/CVD graphene heterostructure. Clearly, the thinner flake is the one shown in panel a).

Chapter 7

Conclusions and future perspectives

As we saw in Chapter 5, the quality of 2D materials grown by Chemical Vapor Deposition goes through two fundamental aspects of catalyst optimization and process optimization.

From one side, the CVD synthesis of monolayer graphene is nowadays a reality and can be produced in large scale with relatively low production cost, making graphene accessible for many companies that could enable the progress towards electronic applications. On the other side, the CVD synthesis of h-BN, as we saw in section 3.2, is only reachable in a laboratory context and is still far from industrial production. Structural defects, contamination, control of number of layers as well as the lack of reproducibility are the most important aspect to consider in order to get a good quality material to introduce into graphene technology.

The PMMA residues, is one of the most relevant sources of doping, which seriously compromise graphene performances. However, with the described PMMA free interface transfer process we can avoid this kind of contamination. Nevertheless, the transfer process must be improved in order to eliminate many other degrading features like trapped water, wrinkles, detachment, etc..

All the h-BN/graphene heterostructures created in this thesis can be used to fabricate electrical devices with optical lithography in order to check many graphene parameters (i.e. mobility, doping, sheet resistance, etc.) which, however, is not the aim of this thesis. Indeed, the substrates used in this context were standard $300nm$ SiO_2, which is not the ideal thickness because the capacity of the oxide would be too small in order to even find the Dirac point of graphene, making the

measurements almost impossible to perform. Therefore, starting from this results, the GRAPHENEA team is going to improve the transfer and create h-BN/graphene heterostructures deposited onto more suitable substrates like SiO_2 $90nm$ or pure Si.

Bibliography

[1] Novoselov K.S., Geim A.K., Morozov S.V., Jiang D., Zhang Y., Dubonos S.V., Grigorieva I.V., Firsov A.A.. *Electric Field Effect in Atomically Thin Carbon Films*. Science 22 OCT: 666-669 (2004).

[2] Geim, A. K. Novoselov, K. S.. *The rise of graphene*. Nature Materials 6, pp. 183 - 191 (2007).

[3] K. S. Novoselov, V. I. Falko, L. Colombo, P. R. Gellert, M. G. Schwab, K. Kim. *A roadmap for graphene*. Nature. Oct 11;490(7419):192-200 (2012) doi: 10.1038/nature11458.

[4] P. R. Wallace. *The band theory of graphite*. Phys. Rev. 71, 622 (1947).

[5] Castro Neto A. H., Guinea F., Peres N.M.R., Novoselov K.S. and A.K. Geim *The electronic properties of graphene*. Rev. Mod. Phys. 81, 109 (2009).

[6] R. Sordan. *Slides teaching material* (2016).

[7] https://en.wikipedia.org/wiki/Boron nitride.

[8] Watanabe K., Taniguchi T. and H. Kanda *Direct-bandgap properties and evidence for ultraviolet lasing of hexagonal boron nitride single crystal.* Nature Materials 3, 404 - 409 (2004).

[9] Jiao J.,Wang X.,Diankov G.,Wang, H. and Dai H. *Facile synthesis of high-quality graphene nanoribbons.* Nature Nanotechnology 5, 321 - 325 (2010).

[10] Giovannetti G., Khomyakov P.A., Brocks G., Kelly P.J. and J. van den Brink *Substrate-induced band gap in graphene on hexagonal boron nitride: Ab initio density functional calculations.*. Phys. Rev B. 76, 073103 (2007).

[11] Young A. F., Dean C. R., Meric I., Sorgenfrei S., Ren H., Watanabe K., Taniguchi T., Hone J., Shepard K. L. and P. Kim *Electronic compressibility of layer-polarized bilayer graphene.* Phys. Rev. B 85, 235458 (2012).

[12] Li Song, Lijie Ci, Hao Lu, Pavel B. Sorokin, Chuanhong Jin, Jie Ni, Alexander G. Kvashnin, Dmitry G. Kvashnin, Jun Lou, Boris I. Yakobson and Pulickel M. Ajayan *Large Scale Growth and Characterization of Atomic Hexagonal Boron Nitride Layers.* Nano Letters 10 (8), 3209-3215 (2010).

[13] Ji Won Suk, Alexander Kitt, Carl W. Magnuson, Yufeng Hao, Samir Ahmed, Jinho An, Anna K. Swan, Bennett B. Goldberg, and Rodney S. Ruoff *Transfer of CVD-Grown Monolayer Graphene onto Arbitrary Substrates* ACS Nano 5 (9), 6916-6924 (2011).

[14] Taeshik Yoon, Woo Cheol Shin, Taek Yong Kim, Jeong Hun Mun, Taek-Soo Kim, and Byung Jin Cho *Direct Measurement of Adhesion Energy of Monolayer Graphene as Grown on Copper and Its Application to Renewable Transfer Process* Nano Letters 12 (3), 1448-1452 (2012).

[15] Jie Song, Fong-Yu Kam, Rui-Qi Png, Wei-Ling Seah, Jing Mei Zhuo, Geok-Kieng Lim, Peter K. H. Ho Lay-Lay Chua *A general method for transferring graphene onto soft surfaces* Nature Nanotechnology 8, 356362 (2013).

[16] Hyun Ho Kim, Yoonyoung Chung, Eunho Lee, Seong Kyu Lee, Kilwon Cho *Water-Free Transfer Method for CVD-Grown Graphene and Its Application to Flexible Air-Stable Graphene Transistors* Advanced Materials, Volume 26, Issue 20, May 28, pp. 32133217 (2014).

[17] Shautsova V., Gilbertson A.M., Black N.C., Maier S.A. and L.F. Cohen. *Hexagonal Boron Nitride assisted transfer and encapsulation of large area CVD graphene* Scientific Reports, Jul 22;6:30210 (2016).

[18] Suk J.W., Lee W.H., Lee J., Chou H., Piner R.D., Hao Y., Akinwande D. and R.S. Ruoff *Enhancement of the Electrical Properties of Graphene Grown by Chemical Vapor Deposition via Controlling the Effects of Polymer Residue* Nano Lett. Apr 10;13(4):1462-7 (2013).

[19] Pirkle A., Chan J., Venugopal A., Hinojos D. and C.W. Magnuson *The effect of chemical residues on the physical and electrical properties of chemical vapor deposited graphene transferred to* SiO_2 Appl. Phys. Lett. 99, September (2011).

[20] Soo Min Kim, Allen Hsu, Min Ho Park, Sang Hoon Chae, Seok Joon Yun, Joo Song Lee, Dae-Hyun Cho, Wenjing Fang, Changgu Lee, Toms Palacios, Mildred Dresselhaus, Ki Kang Kim, Young Hee Lee Jing Kong *Synthesis of large-area multilayer hexagonal boron nitride for high material performance* Nature Communications, 6, 8662 (2015).

[21] Luca Banszerus, Michael Schmitz,Stephan Engels, Jan Dauber, Martin Oellers, Federica Haupt, Kenji Watanabe, Takashi Taniguchi, Bernd Beschoten, Christoph Stampfer *Ultrahigh-mobility graphene devices from chemical vapor deposition on reusable copper* Science Advances, Vol. 1, no. 6, e1500222 (2015).

[22] Cecilia Mattevi, Hokwon Kima and Manish Chhowalla *A review of chemical vapour deposition of graphene on copper* Journal of Materials Chemistry, 21,

3324-3334 (2011).

[23] Xuesong Li, Weiwei Cai, Jinho An, Seyoung Kim, Junghyo Nah, Dongxing Yang, Richard Piner, Aruna Velamakanni *Ultrahigh-mobility graphene devices from chemical vapor deposition on reusable copper* Science, Vol. 324, Issue 5932, pp. 1312-1314, (2009).

[24] Sukang Bae, Hyeongkeun Kim, Youngbin Lee, Xiangfan Xu, Jae-Sung Park, Yi Zheng, Jayakumar Balakrishnan, Tian Lei, Hye Ri Kim, Young Il Song, Young-Jin Kim, Kwang S. Kim, Barbaros zyilmaz, Jong-Hyun Ahn, Byung Hee Hong Sumio Iijima *Roll-to-roll production of 30-inch graphene films for transparent electrodes* Nature Nanotechnology 5, 574578 (2010).

[25] Yao Wen, Xunzhong Shang, Ji Dong, Kai Xu, Jun He and Chao Jiang *Ultraclean and large-area monolayer hexagonal boron nitride on Cu foil using chemical vapor deposition* Nanotechnology, Volume 26, Number 27 (2015).

[26] Xiuju Song, Junfeng Gao, Teng Gao, Yufeng Nie, Jingyu Sun, Yubin Chen, Chuanhong Jin, Feng Ding,Yanfeng Zhang, Zhongfan Liu *Wafer-scale CVD Growth of Monolayer Hexagonal Boron Nitride with Large Domain Size by Cu Foil Enclosure*, mimeo.

[27] Ki Kang Kim, Allen Hsu, Xiaoting Jia, Soo Min Kim, Yumeng Shi, Mario Hofmann, Daniel Nezich, Joaquin F. Rodriguez-Nieva, Mildred Dresselhaus, Tomas Palacios, and Jing Kong *Synthesis of Monolayer Hexagonal Boron Nitride on Cu Foil Using Chemical Vapor Deposition* Nano Letters 12 (1), 161-166 (2012) DOI: 10.1021/nl203249a.

[28] Justin C. Koepke, Joshua D. Wood, Yaofeng Chen, Scott W. Schmucker, Ximeng Liu, Noel N. Chang, Lea Nienhaus, Jae Won Do, Enrique A. Carrion, Jayan Hewaparakrama, Aniruddh Rangarajan, Isha Datye, Rushabh Mehta, Richard T. Haasch, Martin Gruebele, Gregory S. Girolami, Eric Pop, and Joseph W. Lyding *Role of Pressure in the Growth of Hexagonal Boron Nitride Thin Films from Ammonia-Borane* Chem. Mater., 28 (12), pp 41694179 (2016).

[29] Samuel Frueh, Richard Kellett, Carl Mallery, Trent Molter, William S. Willis, Cecil Kingondu, and Steven L. Suib *Pyrolytic Decomposition of Ammonia Borane to Boron Nitride* Inorganic Chemistry, 50 (3), 783-792 (2011) DOI: 10.1021/ic101020k.

[30] www.sil-tronix-st.com

[31] K. S. Novoselov, D. Jiang, R. Yang, T. J. Booth, and A. K. Geim *Making graphene visible* Applied Physics Letters 91, 063124 (2007).

[32] Gorbachev, R. V., Riaz, I., Nair, R. R., Jalil, R., Britnell, L., Belle, B. D., Hill,

E. W., Novoselov, K. S., Watanabe, K., Taniguchi, T., Geim, A. K. and Blake, P. *Hunting for Monolayer Boron Nitride: Optical and Raman Signatures* Small, 7: 465468. (2011) doi:10.1002/smll.201001628.

[33] Jang A.R., Hong S., Hyun C., Yoon S.I., Kim G., Jeong H.Y., Shin T.J., Park S.O., Wong K., Kwak S.K., Park N., Yu K., Choi E., Mishchenko A., Withers F., Novoselov K.S., Lim H. and H.S. Shin *Wafer-Scale and Wrinkle-Free Epitaxial Growth of Single-Orientated Multilayer Hexagonal Boron Nitride on Sapphire* Nano Letters, 16 (5), 3360-3366 (2016) DOI: 10.1021/acs.nanolett.6b01051.

[34] Boo J., Rohr C. and W. Ho *MOCVD of BN and GaN thin films on silicon: new attempt of GaN growth with BN buffer layer* Journal of Crystal Growth, Volumes 189190, 15 June, Pages 439-444 (1998).

[35] Castellanos-Gomez A., Buscema M., Molenaar R., Singh V., Janssen L., van der Zant H.S.J. and G.A. Steele *Deterministic transfer of two-dimensional materials by all-dry viscoelastic stamping* 2D Materials, Volume 1, Number 1 (2014).

[36] Meitl M.A.,, Zhu Z.T, Kumar V., Lee K.J, Feng X., Huang Y.Y., Adesida I., Nuzzo R.G. and J.A. Rogers *Transfer printing by kinetic control of adhesion to an elastomeric stamp* Nature Materials 5, 33 - 38 (2006).

[37] www.aixtron.com

[38] www.witec.de

[39] www.bruker.com

[40] www.agilent.com

[41] www.specs.de

[42] www.graphenesupermarket.com

[43] www.nitto.com

[44] www.hqgraphene.com

[45] www.gel-pak.com

[46] www.canon.com